Northern Hemisphere Winter Atmospheric Transient Eddy Heat Fluxes and the Gulf Stream and Kuroshio–Oyashio Extension Variability

YOUNG-OH KWON AND TERRENCE M. JOYCE

Woods Hole Oceanographic Institution, Woods Hole, Massachusetts

(Manuscript received 3 September 2012, in final form 30 May 2013)

ABSTRACT

Spatial and temporal covariability between the atmospheric transient eddy heat fluxes (i.e., $\langle v'T' \rangle$ and $\langle v'q' \rangle$) in the Northern Hemisphere winter (January–March) and the paths of the Gulf Stream (GS), Kuroshio Extension (KE), and Oyashio Extension (OE) are examined based on an atmospheric reanalyses and ocean observations for 1979–2009.

For the climatological winter mean, the northward heat fluxes by the synoptic (2–8 days) transient eddies exhibit canonical storm tracks with their maxima collocated with the GS and KE/OE. The intraseasonal (8 days–3 months) counterpart, while having overall similar amplitude, shows a spatial pattern with more localized maxima near the major orography and blocking regions. Lateral heat flux divergence by transient eddies as the sum of the two frequency bands exhibits very close coupling with the exact locations of the ocean fronts.

Linear regression is used to examine the lead–lag relationship between interannual changes in the northward heat fluxes by the transient eddies and the meridional changes in the paths of the GS, KE, and OE, respectively. One to three years prior to the northward shifts of each ocean front, the atmospheric storm tracks shift northward and intensify, which is consistent with wind-driven changes of the ocean. Following the northward shifts of the ocean fronts, the synoptic storm tracks weaken in all three cases. The zonally integrated northward heat transport by the synoptic transient eddies increases by ~5% of its maximum mean value prior to the northward shift of each ocean front and decreases to a similar amplitude afterward.

1. Introduction

One of the most fundamental aspects of earth's climate is the latitudinal dependence of the top-of-the-atmosphere radiative imbalance and resulting equator-to-pole heat transport by the ocean and atmosphere. In the Northern Hemisphere, the ocean and atmosphere carry nearly equal amounts of the heat northward in the tropics (up to ~15°N), while the atmosphere transports most of the heat poleward of ~40°N (e.g., Trenberth and Caron 2001). In between the two latitude bands, the ocean hands over most of the heat to the atmosphere. The ocean-to-atmosphere heat transfer is concentrated near the western boundary current (WBC) region [i.e., the Gulf Stream (GS) and Kuroshio–Oyashio Extension (KOE)], which is signified by the largest ocean-to-atmosphere heat fluxes in the globe in the annual-mean sense as well as for the interannual variability. Another important contrast between the ocean and atmosphere is the very different role of mean circulations and eddies. In the ocean, most of the northward heat transport is carried by the mean large-scale circulation especially in the extratropics (Jayne and Marotzke 2002; Volkov et al. 2008; Johns et al. 2011), while the transient eddies play a significant role in the atmospheric heat transport especially north of ~40°N (Priestley 1949; Lorenz 1967; Trenberth and Stepaniak 2003a). Therefore, the interaction between the large-scale ocean circulation and the atmospheric transient eddies near the GS and KOE must be a crucial aspect of the northward heat transport.

Large meridional gradients of latent and sensible heat fluxes across the strong SST fronts along the GS and KOE may act to anchor the atmospheric storm tracks by maintaining baroclinicity in the overlying atmosphere (Hoskins and Valdes 1990; Nakamura et al. 2004). Storm tracks in the North Atlantic and North Pacific based on the bandpass-filtered statistics for the synoptic time scale [~(2–8) days] are indeed collocated with the GS and KOE (Blackmon 1976; Blackmon et al. 1977; Raphael

Corresponding author address: Young-Oh Kwon, Physical Oceanography Department, Woods Hole Oceanographic Institution, MS 21, Woods Hole, MA 02543.
E-mail: yokwon@whoi.edu

DOI: 10.1175/JCLI-D-12-00647.1

1997; Chang et al. 2002). In addition, storm-track statistics based on the tracking of individual low-pressure systems reveal the maximum occurrence and growth rate of the storms in these western boundary current regions (Hoskins and Hodges 2002).

On the other hand, atmospheric intraseasonal [~(8–90) days or ~8 days and longer and often referred to as low frequency] transient eddy variability is more pronounced in the eastern basins near the downstream exit region of the synoptic storm track (Blackmon 1976; Blackmon et al. 1977, 1984; Kushnir and Wallace 1989). Some studies suggested the causal relationship between the upstream synoptic variability and the downstream intraseasonal variability with a viewpoint that the synoptic variability develops and propagates rapidly in the upstream while slowly decaying in the downstream exit region to contribute to the intraseasonal variability (Dole and Black 1990; Nakamura and Wallace 1990). Intraseasonal variability contains much greater year-to-year variance than the synoptic time scale and often is related to the atmospheric teleconnection patterns (Blackmon et al. 1984; Kushnir and Wallace 1989; Newman et al. 2012).

While the atmospheric heat flux by the synoptic transient eddies is largest near the GS and KOE along the storm tracks (Blackmon et al. 1977; Raphael 1997; Trenberth and Stepaniak 2003b), the heat flux by the intraseasonal transient eddies exhibits smaller zonal scale and more localized patterns, often to the north and south of the storm tracks (Blackmon et al. 1977; Dole and Black 1990; Newman et al. 2012). However, Trenberth and Stepaniak (2003a,b) demonstrated that the compensation between the heat fluxes in the high and low frequencies (i.e., within-monthly transient and lower-frequency quasi-stationary including mean components in their analyses) makes a seamless smooth spatial pattern of total meridional heat flux and zonally integrated meridional heat transport.

Recent advances in the satellite observation and atmospheric reanalyses allowed further progress of our understanding in how the ocean and atmosphere interacts in these regions of strong ocean fronts. Minobe et al. (2008) demonstrated that the strong gradient of the SST across the GS leads to surface wind convergence, which anchors a narrow band of precipitation along the GS. Furthermore, the associated upward motion and cloud formation exhibited the influence of the GS extends into the upper troposphere in the climatological annual-mean fields. In a follow-up study, Minobe et al. (2010) examined the seasonality of this mean atmospheric response. They found that deep heating dominates along the Florida Current and upstream GS in summer, while the shallow heating dominates in winter along the GS. Several subsequent studies showed similar influence of the Kuroshio in the North Pacific (Toginaga et al. 2009; Xu et al. 2011; Sasaki et al. 2012).

In addition to the climatological mean impact of the strong ocean fronts up to the upper troposphere, Joyce et al. (2009) showed that the year-to-year changes in the winter surface storm activity in each basin (measured by the variances in the 2–8-day synoptic band of surface wind, their vorticity, and divergence as well as the surface turbulent fluxes) covaries with the changes in the latitude of the GS and Kuroshio Extension (KE), respectively. If the interannual variability of the GS and KOE is felt by the atmosphere beyond the marine boundary into the troposphere as shown in the climatological-mean fields, the impact could reach beyond the narrow ocean frontal regions through the changes in the large-scale atmospheric circulation (Kelly et al. 2010; Kwon et al. 2010). While many climate model simulations suggest such feedback from strong ocean frontal variability to the large-scale atmospheric circulation (e.g., Taguchi et al. 2009; Kwon et al. 2011), corresponding observational evidences are still very limited.

Nevertheless, the GS, KE, and Oyashio Extension (OE) exhibit prominent interannual-to-decadal variability, especially for the fluctuation in the meridional position of these ocean fronts (Joyce et al. 2000; Qiu and Chen 2005; Joyce et al. 2009; Frankignoul et al. 2011). KE changes have been explained as the response to the basin-scale wind stress curl changes associated with the Aleutian low fluctuations, primarily the meridional shifts, with 3–5-yr delay via the baroclinic Rossby wave adjustment (Deser et al. 1999; Seager et al. 2001; Qiu and Chen 2005; Qiu et al. 2007; Kwon and Deser 2007). Studies suggest that the OE also responds to the basin-scale wind stress curl changes but much faster than KE as the barotropic Rossby wave adjustment dominates (Qiu 2002; Nonaka et al. 2008; Frankignoul et al. 2011). The GS path fluctuation is also shown to be driven by the changes in the wind stress curl forcing associated with the North Atlantic Oscillation (NAO) with the peak lag correlation found when NAO leads the GS by 1 yr (Joyce et al. 2000), as well as by the changes in the equatorward Labrador Slope Water transport as a part of the Atlantic meridional overturning circulation (Peña-Molino and Joyce 2008; Joyce and Zhang 2010).

In this study, we examine the covariability between the winter [January–March (JFM)] atmospheric eddy heat and moisture fluxes by transient eddies from the surface to 50 hPa in the whole Northern Hemisphere and the GS, KE, and OE based on an atmospheric reanalysis and the ocean frontal indices from observation. First, we examine the climatological mean winter transient eddy fluxes with the focus on how their spatial

distribution is coupled to the mean large-scale ocean circulation pattern. Then, the covariability between the two in the interannual-to-decadal time scale is investigated with the primary emphasis on how the changes in the GS path impact the atmospheric synoptic transient eddy fluxes.

2. Data and method

a. Atmospheric variables

Daily mean variables in winter (January–March) from the Modern-Era Retrospective Analysis for Research and Applications (MERRA; Rienecker et al. 2011) for the recent 31 years (1979–2009) are used in this study. MERRA has ½° latitude and ⅔° longitude horizontal resolution, and our analysis is confined to the Northern Hemisphere. (The figures are plotted for the region north of 20°N, unless noted otherwise.) Even though MERRA has 72 hybrid sigma coordinate vertical levels, data at only 6 selected pressure levels (i.e., 100, 200, 250, 500, and 850 hPa and sea level) are used.

Daily variables are high-pass filtered at 8 days using the Lanczos filter with 15 weights (Duchon 1979) to calculate the synoptic transient anomaly. The result is not sensitive to the number of weights used here. Then the daily synoptic transient anomaly is subtracted from the JFM mean value in each respective year to get the intraseasonal transient anomaly for the three winter months. Note that the analysis in this paper is confined to the winter months.

b. Calculation of transient eddy heat fluxes and heat flux divergences

First, as described above, each daily mean variable at our six selected levels, extracted for each winter (e.g., JFM 1979), is decomposed into three terms: that is, the 3-month mean $\langle x\rangle$, synoptic (2–8 days) transient anomaly x'^{s}, and intraseasonal (8 days–3 months) transient anomaly x'^{i}. For example, daily meridional winds v for the three winter months are decomposed into

$$v = \langle v\rangle + v'^{s} + v'^{i}. \tag{1}$$

The seasonal mean could be further decomposed into the zonal-mean and stationary eddy anomalies. However, focus of this study will be limited to the transient eddies.

Then, the covariances in each 3-month period are calculated. For example, the covariance between the meridional wind and temperature is decomposed into

$$\langle vT\rangle = \langle v\rangle\langle T\rangle + \langle v'^{s}T'^{s}\rangle + \langle v'^{i}T'^{i}\rangle + \langle v'^{s}T'^{i}\rangle + \langle v'^{i}T'^{s}\rangle. \tag{2}$$

Therefore, the total transient eddy term ($\langle v'T'\rangle = \langle vT\rangle - \langle v\rangle\langle T\rangle$) is composed of the synoptic transient eddy term $\langle v'^{s}T'^{s}\rangle$ and the intraseasonal transient eddy term $\langle v'^{i}T'^{i}\rangle + \langle v'^{s}T'^{i}\rangle + \langle v'^{i}T'^{s}\rangle$. Although the cross product terms are negligible, they are included in the intraseasonal transient eddy term for completeness. These covariance terms are multiplied by the seasonal-mean density ($\rho = \sim 1.3\,\mathrm{kg\,m^{-3}}$) and specific heat ($C_p = \sim 1000\,\mathrm{J\,kg^{-1}\,K^{-1}}$), which are spatially and vertically varying as functions of seasonal-mean pressure, temperature, and specific humidity and called the meridional sensible heat flux by transient eddies ($=\rho C_P\langle v'T'\rangle$).

The meridional sensible heat flux terms in synoptic and intraseasonal bands are calculated for each three winter months for 1979–2009 to result in a time series: one value for each of the 31 years, for the synoptic and intraseasonal bands, respectively, at each spatial grid point and level. The 31-yr means and their interannual standard deviation are analyzed in the following sections.

Likewise, the meridional latent heat fluxes by transient eddies ($=\rho L\langle v'q'\rangle$) are calculated for synoptic and intraseasonal bands from the covariance between the meridional wind and specific humidity q multiplied by the seasonal-mean density and heat of vaporization ($L = \sim 2.5\times 10^{3}\,\mathrm{J\,kg^{-1}}$).

Vertically integrated whole atmospheric column fluxes ($\mathrm{W\,m^{-1}}$) for the latent and sensible components, respectively, (and also the sum) are again calculated separately for the two frequency bands:

$$\frac{1}{g}\int_{50\,\mathrm{hPa}}^{\text{Sea-level}} (C_P\langle v'T'\rangle + L\langle v'q'\rangle)\,dp. \tag{3}$$

Note that the vertical integrations extend to 50 hPa by assuming linear decrease from values at 100 hPa to zero at 50 hPa. A trapezoidal scheme was used for vertical integration based on the pressure levels selected for analysis. Then, the zonally integrated meridional heat transport by transient eddies [petawatt (PW)] is calculated by zonally integrating Eq. (3) along each latitude band. The spatial patterns are shown with the vertically integrated fields unless noted otherwise.

In addition, the lateral heat flux divergences by transient eddies are calculated for each component and frequency band [e.g., $\rho C_P\langle \partial(u'^{s}T'^{s})/\partial x + \partial(v'^{s}T'^{s})/\partial y\rangle$] and vertically integrated.

c. Oceanic indices

Indices for the interannual-to-decadal meridional shift in the position of the GS, KE, and OE, respectively, are calculated from the available observations to examine their covariability with the atmospheric transient eddy heat fluxes. All three indices are the principal component (PC) time series of the respective leading mode of the empirical orthogonal function (EOF) for the

time-varying meridional position of the corresponding ocean front.

The GS position is defined based on the latitude of the 15°C isotherm at 200 m in 55°–75°W using historical temperature measurements from primarily the *World Ocean Database 2009* (Boyer et al. 2009), with seasonal resolution since 1954 (Joyce et al. 2000). In this study, the GS index (GSI) in the overlapping period with MERRA from 1979 to 2006 is used. The KE index (KEI) is defined similarly based on the latitude of the 14°C isotherm at 200 m in 142°–160°E from 1980 to 2006 with seasonal resolution (Joyce et al. 2009).

Unlike the KE and GS, the OE front is mostly confined at the surface within the mixed layer (Yasuda 2003; Nonaka et al. 2006). Therefore, the OE position is defined as the latitude of the maximum meridional SST gradient (dSST/dy) at each longitude from 145° and 170°E based on the monthly mean of the National Oceanic and Atmospheric Administration (NOAA) optimum interpolation ¼° daily SST [OISST; Advanced Very High Resolution Radiometer (AVHRR)-only product; Reynolds et al. 2007] for 1982–2008 (Frankignoul et al. 2011). The monthly OE index (OEI) is then seasonally averaged to be compared with the winter transient eddy heat flux.

Note that the indices are not fully statistically independent from each other, as the variability in these ocean fronts could be physically correlated [also see the discussion in section 5e of Kwon et al. (2010)]. Simultaneous correlations between the KE index and the other two indices in winter are statistically not significant at the 90% level ($r < 0.3$ for both cases). However, the KE and GS indices are much more correlated ($r = 0.68$) for the latter half of the overlapping period. Therefore, the relationship between the KE and GS is nonstationary. In addition, the correlation between the winter GS and OE indices is 0.39, barely significant at the 90% level.

The mean positions of the three oceanic fronts (GS, KE, and OE) will be indicated as thick curves in all of the following spatial maps as a reference.

d. Lag regressions

The lag regressions of the 31-yr time series of the winter transient eddy heat fluxes on the GS, KE, and OE indices, respectively, are calculated after the linear trends are removed from both the transient eddy heat fluxes and ocean indices for the overlapping periods. In addition, the variability correlated with the tropical SST variability is removed from all the transient eddy heat fluxes before the regressions are calculated to properly estimate the responses of the transient eddy heat fluxes to the extratropical ocean frontal variability (Frankignoul et al. 2011). Teleconnections originating from the tropics are the largest source of persistent variability in interannual and longer time scales resulting in correlated persistent anomalies in the midlatitude ocean and atmosphere. Those signals may show up in the lag regression with the ocean leading the atmosphere by longer than a season and confuse the causality. Without those remote signals, the persistence of the atmospheric intrinsic variability in the midlatitude is only a couple of weeks. Therefore, the lag regression with the ocean leading by a year or longer can be interpreted as the atmospheric response to the ocean frontal variability (Frankignoul et al. 1998; von Storch 2000).

Tropical-correlated variability is calculated as the linear regression of the transient eddy heat fluxes on the PC time series for the three leading EOFs of the JFM SST in the tropical Indo-Pacific (15°S–15°N) and then subtracted from the original transient eddy heat fluxes. Likewise the regressions on the three leading PCs of the tropical Atlantic SST are removed additionally (Frankignoul and Kestenare 2002; Frankignoul et al. 2011). Note that the tropical signal is removed only for the regression analyses presented in section 3c but not for the mean and interannual variability in sections 3a and 3b.

The statistical significance of the regression or correlation coefficients is assessed according to a two-sided Student's t test using an effective temporal degree of freedom taking into account serial autocorrelation (Trenberth 1984; Bretherton et al. 1999).

e. Other data and regressions

Daily indices for the Pacific–North American (PNA) teleconnection and the Arctic Oscillation (AO) for the corresponding period were downloaded from the NOAA Climate Prediction Center (http://www.cpc.ncep.noaa.gov/). Note that these daily PNA and AO indices are nearly orthogonal ($r = \sim -0.1$) but not completely since the definition used by the Climate Prediction Center does not require them to be orthogonal.

Regression of the daily meridional wind and temperature at 850 hPa on the PNA and AO, respectively, is calculated for individual winters (JFM) after the linear trends for the 3 months in all variables are removed. For these regressions, the tropical influence is not removed.

3. Results

a. Mean spatial patterns

The 31-yr mean pattern of the winter (JFM) vertically integrated meridional heat fluxes by the transient eddies in the synoptic band exhibits a canonical storm-track distribution with maximum amplitudes near the GS and KOE (Figs. 1a–c; Blackmon et al. 1977). Collocations of

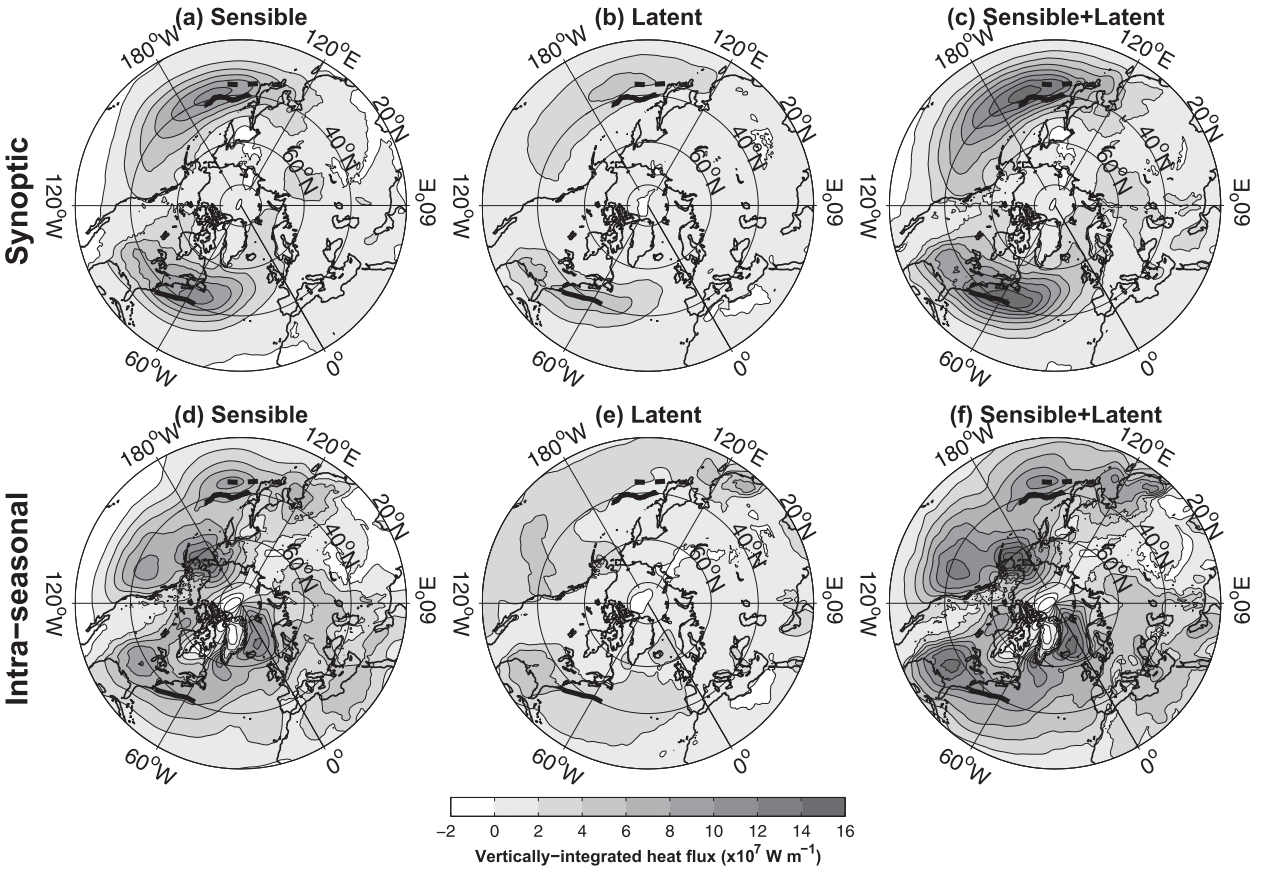

FIG. 1. The 31-yr mean winter (JFM) vertically integrated meridional heat fluxes by transient eddies in (top) synoptic and (bottom) intraseasonal bands. (a),(d) Sensible heat fluxes, (b),(e) latent heat fluxes, and (c),(f) sensible + latent heat fluxes. Contour intervals are 2×10^7 W m^{-1}. The mean positions of the GS and OE are indicated by thick black curves and KE with thick dashed curves. The projection is for the Northern Hemisphere poleward of 20°N with the latitude circles at 40°, 60°, and 80°N.

the storm-track maxima and the mean location of the GS and KOE are particularly clearly shown in Figs. 1a–c, with the mean location of the ocean fronts (from independent data) indicated by thick black lines. Collocations are probably due to the strong meridional gradient of surface air temperature and humidity associated with the GS and KOE acting to anchor the storm track (Hoskins and Valdes 1990; Nakamura et al. 2004). The maximum amplitudes are $\sim 10 \times 10^7$ and $\sim 4 \times 10^7$ W m^{-1} for the sensible and latent components, respectively, with similar amplitudes in the Pacific and Atlantic in both components. The values are consistent with previous estimates (e.g., Peixoto and Oort 1992; Raphael 1997). Note that the maxima in the latent component are located slightly to the south of the sensible counterparts due to the subtropical origin of moisture.

A markedly different spatial pattern is found in the intraseasonal time scale (Figs. 1d–f). Unlike the synoptic time scale, the winter mean heat fluxes by the transient eddies exhibit much more localized maxima, generally near the major orography (i.e., downstream of the Rockies, Greenland, and Himalayas but also near the Bering Strait, off the west coast of the North America, and in the KOE). These local maxima are especially apparent with the sensible component but also present in the latent part. The latent component also indicates the moisture sources, such as the Gulf of Mexico. Note that the maximum near the Gulf of Mexico in the latent component is located to the south of the corresponding maximum in the sensible component, as is the case for the synoptic time scale. These local maxima are enveloped with slightly elevated heat flux that in general coincides with the storm track shown in the synoptic band (e.g., from the lee of the Rockies to the east of Greenland).

The spatial pattern in the intraseasonal time scale is shaped by the variability in the quasi-stationary waves associated with the leading modes of atmospheric variability (e.g., the PNA and AO), which exhibit significant variance in the intraseasonal band (Kushnir and Wallace

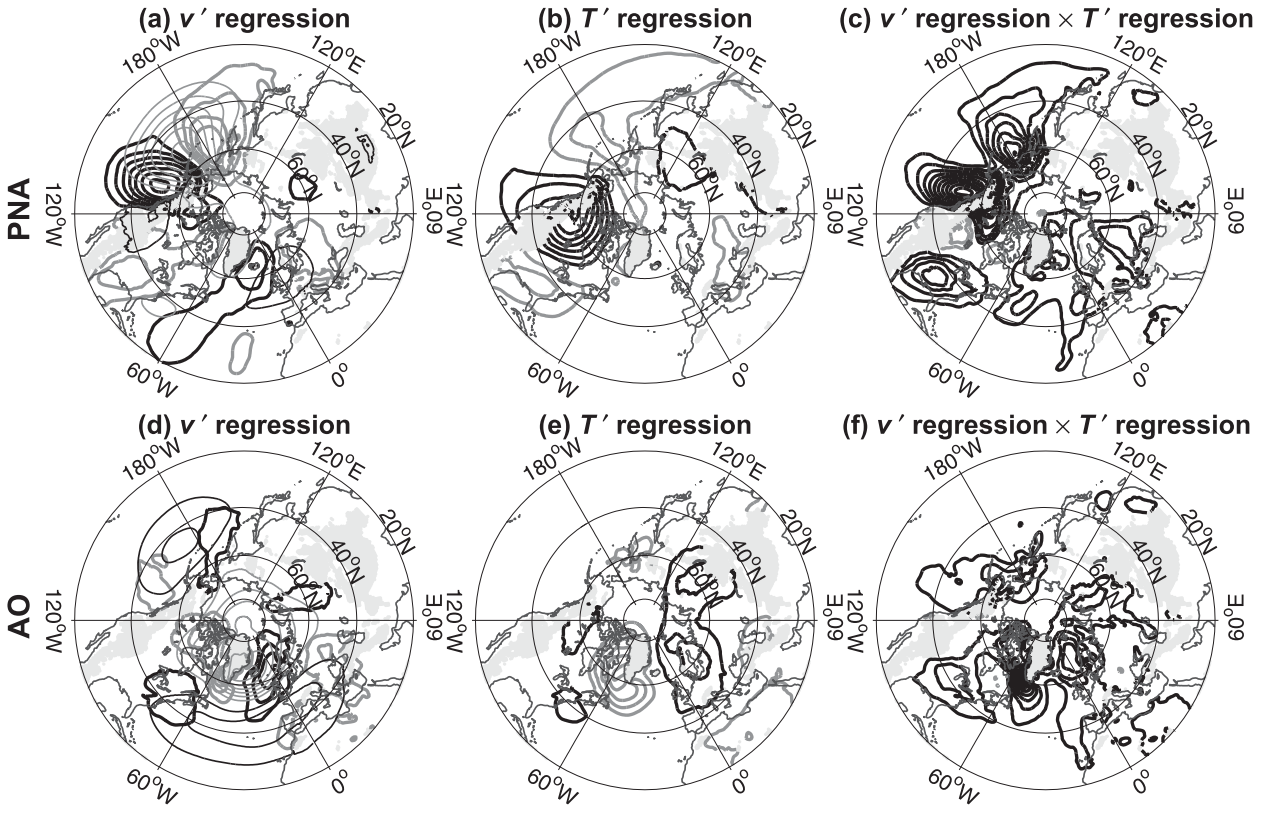

FIG. 2. The 31-yr mean of the regressions for winter (JFM) intraseasonal daily fields at 850 hPa on daily index of (top) PNA and (bottom) AO, respectively. Each variable is filtered for the intraseasonal band and the linear trend is removed for every 3 months. Then, the regressions are calculated independently for each winter and the 31 regressions are averaged for the (a),(d) geopotential heights (H; thin contours) and meridional velocity (v; thick contours) and (b),(e) temperature (T). (c),(f) The regressions for the meridional velocity and temperature are multiplied for each winter and then 31 regressions are averaged. Positive (negative) values are contoured in black (gray) lines. Zero contours are suppressed. Contour intervals are 10 m, 0.5 m s^{-1}, 0.5 K, and 0.5 $\times$ 10^6 W m^{-2}, respectively. Gray shadings indicate the region where the mean surface pressure is less than 850 hPa.

1989; Newman et al. 2012). Figures 2a and 2b show the strengthened Aleutian low associated with the positive PNA accompanies cold southerly and warm northerly anomalies in the western and eastern half of the anomalous low pressure, respectively. The covariability of daily v'^i and T'^i associated with the PNA is then examined from the product of individual regression, which reveals the positive covariance (i.e., northward heat transport) near the Bering Strait and off the west coast of North America (Fig. 2c). Local positive maxima associated with the PNA are also found downstream of the Rockies and much weaker yet also east of Greenland and Himalayas. Similarly, the variability associated with the AO in the intraseasonal band explains local maxima near the Bering Strait, downstream of Greenland, the Rockies, and the Himalayas (Figs. 2d–f). These plots based on the 850-hPa level are representative of different levels as well. The AO regressions, however, show the maximum covariability over the Labrador Sea, which is not as apparent in the transient eddy heat flux map in Figs. 1d–f. Unlike the intraseasonal band, projections of daily variables on PNA and AO are negligible in the synoptic band (not shown).

Averaged vertical profiles over the latitude band encompassing the maximum amplitudes (30°–50°N; which contains ~55% of the synoptic and ~33% of the intraseasonal vertically integrated meridional heat fluxes by transient eddies in the whole Northern Hemisphere) exhibit the primary maximum transient eddy heat flux at 850 hPa associated with the near-surface storm track and the secondary maximum near 200 hPa near the tropopause in both time scales, as well as both the sensible and latent heat components (Fig. 3). Unlike the momentum fluxes (e.g., $\langle v'u' \rangle$), the heat fluxes have their maximum near the low-level jet because of the greater temperature and humidity variability near the surface. The two time scales exhibit comparable amplitude throughout the atmospheric column. On the other hand, the contribution from the latent heat flux is only two-thirds that of the sensible heat flux and decreases dramatically as

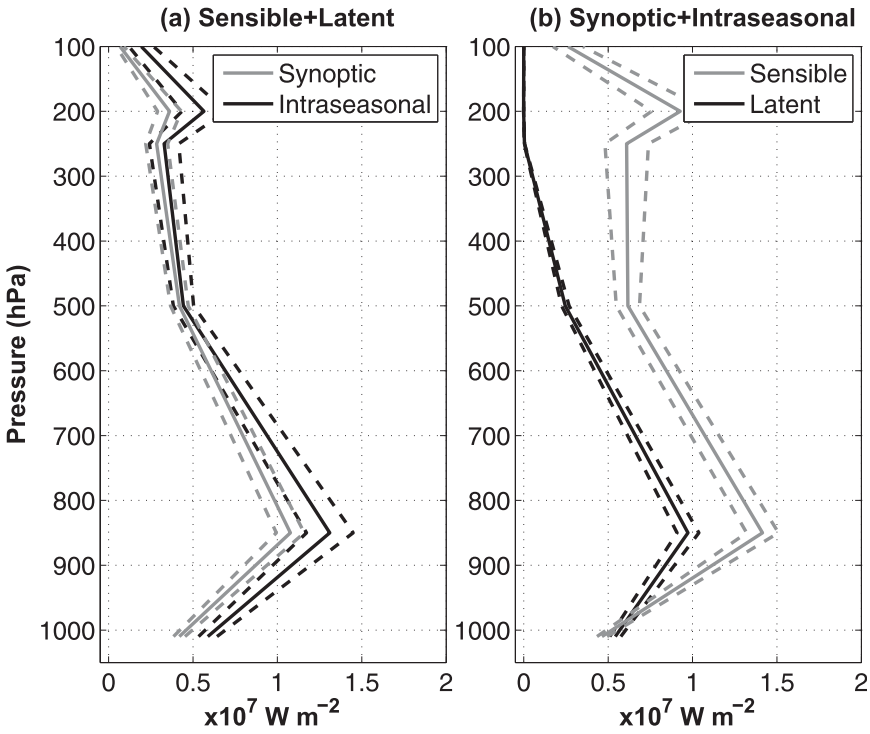

FIG. 3. Vertical profiles of winter (JFM) meridional heat fluxes by transient eddies averaged over the zonal band between 30° and 50°N for (a) sensible + latent components and (b) synoptic + intraseasonal bands. The thick lines are for the 31-yr mean, and the dashed lines indicate one standard deviation ranges.

the height increases to become negligible at 250 hPa and above as the upper atmosphere lacks moisture.

Zonal integration of the meridional heat flux by transient eddies (i.e., the zonal integration of Fig. 1) results in the familiar net northward heat transport by atmospheric transient eddies as a function of latitude in petawatts (Fig. 4; cf. Trenberth and Stepaniak 2003b). Maximum total heat transport by transient eddies is ~3.7 PW near 35°–40°N, of which the half is from the synoptic band (Fig. 4a). The intraseasonal band, however, contributes to a much broader latitude range, while the synoptic contribution is narrowly concentrated around the maximum heat transport latitude. Sensible and latent components make up two-thirds and one-third of the maximum heat transport, respectively (Figs. 4b,c). On the other hand, the latent component, especially in the intraseasonal band, is the primary contributor in the tropics up to ~25°N, reflecting the dominant tropical/subtropical source of moisture (Fig. 4c), while the relative contribution from the sensible component increases monotonically poleward from there on.

The northward heat transport by the transient eddies redistributes the excessive heat from the tropics to the high latitudes, one of the fundamental aspects of Earth's climate. The meridional gradients of the northward heat transport indicate the maximum heat flux convergence by the synoptic and intraseasonal eddies in 40°–60°N and poleward of 65°N, respectively (Fig. 4a). The map of vertically integrated lateral heat flux divergence by the transient eddies reinforces this observation (Fig. 5). Synoptic eddies carry heat from the warmer subtropical gyres south of the KOE and GS to the colder subpolar gyres side in a relatively narrow latitude range between 25° and 55°N (Fig. 5a). As pointed out already, the collocations between the transition from the atmospheric transient eddy heat flux divergence to convergence and the mean positions of the KOE and GS are clearly shown, considering independent sources of the data. In particular, the maximum heat flux divergence is tightly related to the maximum surface heat flux from the ocean to the atmosphere just south of the GS and KE. In contrast, the intraseasonal variability exhibits the maximum heat flux divergence farther south (e.g., the Gulf of Mexico) and also in the eastern portion of the basin, especially west of the British Isles, while the maximum convergence is found in the Arctic Circle (Fig. 5b). Furthermore, those two time scales with rather distinct spatial patterns reveal a seamless spatial distribution as a total (Fig. 5c). Note that the northern edge of the heat flux divergence region in the North Atlantic tracks the

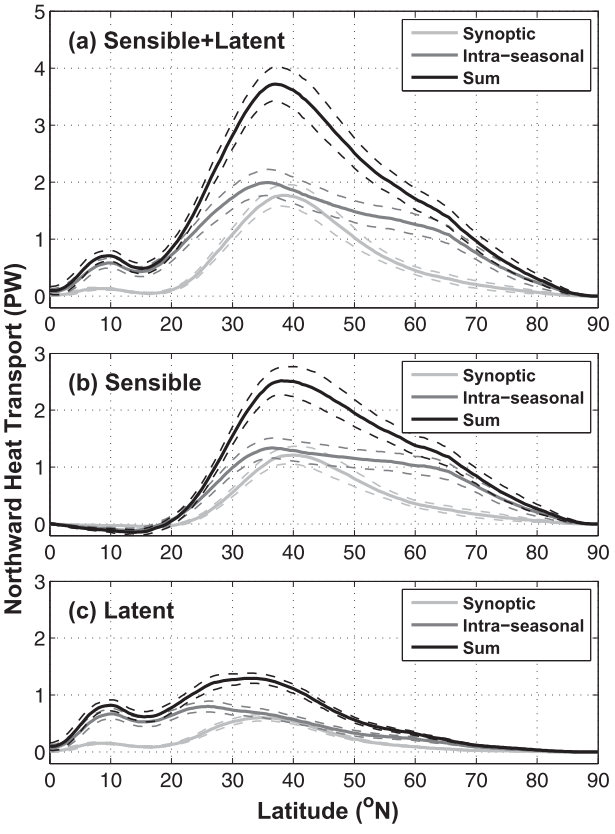

FIG. 4. Winter (JFM) zonally integrated northward heat transport by transient eddies for (a) sensible + latent, (b) sensible, and (c) latent components. The solid curves indicate 31-yr mean and the dashed lines are for one standard deviation ranges.

position of the SST front along the North Atlantic Current (NAC). In the North Pacific, the northern edge of the heat flux divergence is close to the KE latitude because of the greater contribution from the latent surface heat flux, while the primary SST front is located near the OE (Kelly et al. 2010; Frankignoul et al. 2011).

b. *Interannual variability*

Maximum interannual variability of the JFM meridional heat flux by transient eddies for the synoptic time scale is found slightly north and downstream of the maximum in the mean fields in both the Atlantic and Pacific (Figs. 6a–c). The maximum standard deviations are $\sim 3 \times 10^7\,\mathrm{W\,m^{-1}}$, which is about 20% of the maximum mean values. The interannual variability in the sensible heat flux is more than twice that in the latent counterpart.

In the intraseasonal time scale, the interannual standard deviations are nearly two times greater than those in the synoptic band (Figs. 6d–f), while the maximum mean values in the two frequency bands are comparable (Fig. 1). Thus, the amplitudes of the interannual variability

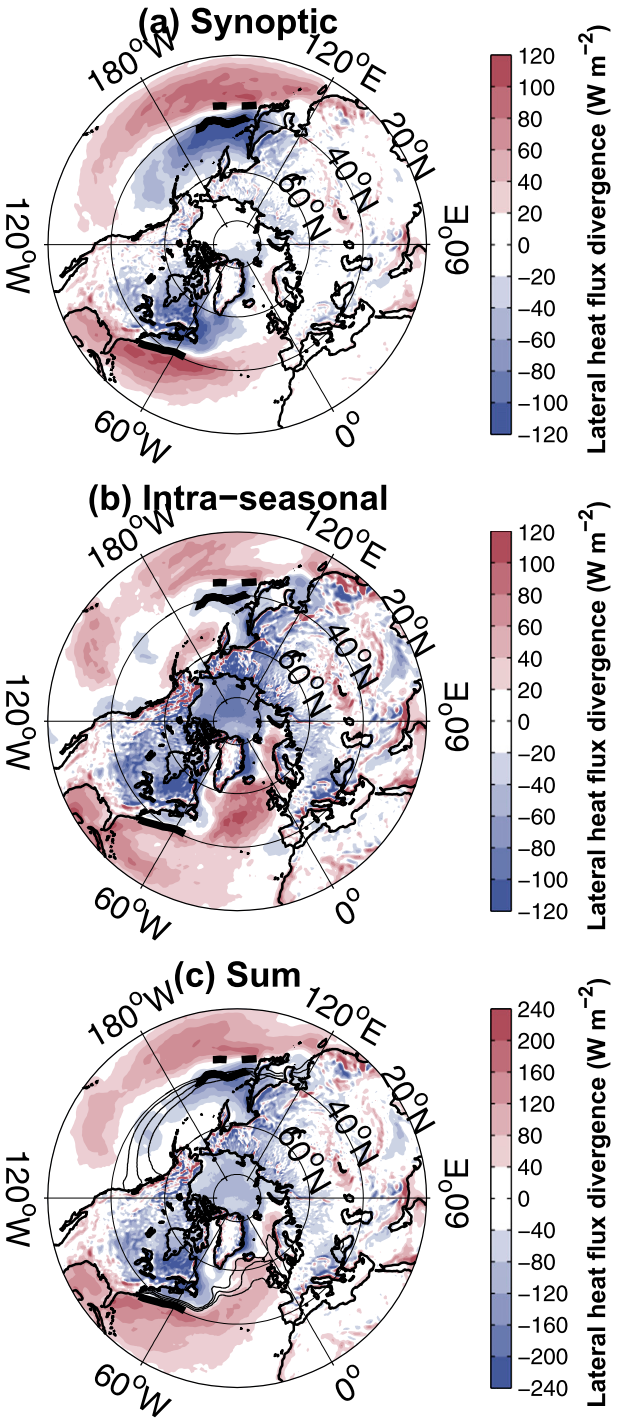

FIG. 5. The 31-yr mean winter (JFM) vertically integrated lateral heat flux divergence by transient eddies as the sum of the sensible and latent components in the (a) synoptic band, (b) intraseasonal band, and (c) sum of two bands. Contour intervals are $20\,\mathrm{W\,m^{-2}}$ for the top two panels and $40\,\mathrm{W\,m^{-2}}$ for the bottom panel. Isotherms of the mean JFM SST for 6°, 8°, and 10°C are plotted with thin black lines. The mean positions of the GS and OE are indicated by thick black curves, and KE is indicated by thick dashed curves.

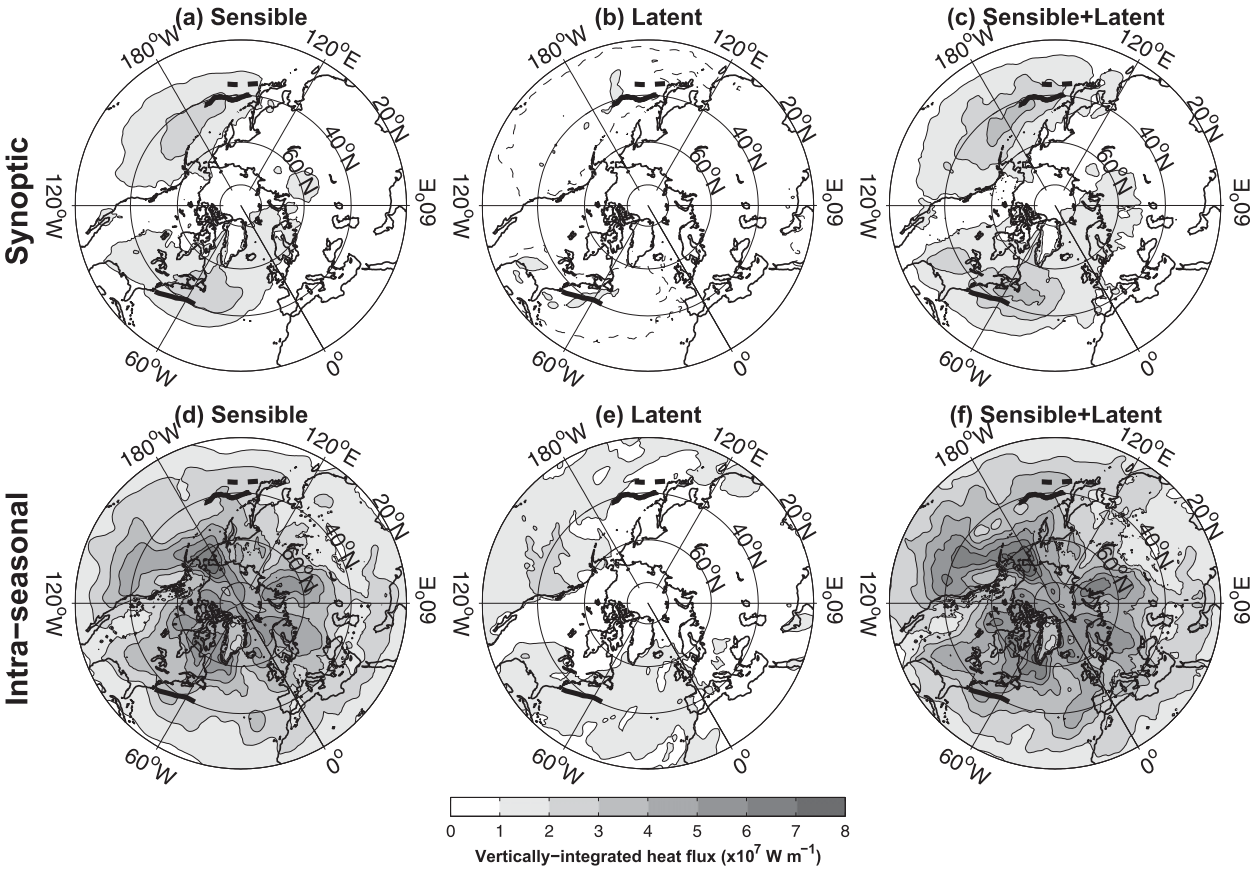

FIG. 6. Interannual standard deviation of 31 winter (JFM) mean vertically integrated meridional heat flux by transient eddies in (top) synoptic and (bottom) intraseasonal bands. (a),(d) Sensible heat fluxes, (b),(e) latent heat fluxes, and (c),(f) sensible + latent heat fluxes. Contour intervals are $1 \times 10^7\,\mathrm{W\,m^{-1}}$. In addition, $0.5 \times 10^7\,\mathrm{W\,m^{-1}}$ contour is added as dashed line in (b). The mean positions of the GS and OE are indicated by thick black curves, and KE is indicated by thick dashed curve.

are about half the mean amplitudes in the intraseasonal time scale. The maxima in the standard deviation are mostly concentrated around the Arctic along ~60°N in the form of a circumpolar zonal wavenumber 4 pattern. Note that there is not any noticeable local maximum variability found near the Rockies, unlike the mean pattern. Latent heat flux variability exhibits clear local maxima off the U.S. Northwest but is overall weaker than the sensible components in this time scale (Fig. 6e).

Interestingly, the interannual variability in the lateral heat flux divergences in the two time scales reveals somewhat similar spatial patterns (Fig. 7), unlike what the other fields have shown so far. Interannual variability is primarily concentrated around the GS–NAC and KOE in both time scales, with slight downstream locations for the intraseasonal band. The standard deviation in the intraseasonal band is more than two times greater than that in the synoptic band (i.e., ~90 versus ~40 $\mathrm{W\,m^{-2}}$), unlike the comparable amplitudes in the mean fields. The sum of the two time scales, once again, exhibits seamless patterns centered along the SST fronts in both the North Atlantic and North Pacific (Fig. 7c).

c. *Covariability with the GS, KE, and OE*

Now we will examine how much of the interannual variability of the winter meridional heat fluxes by transient eddies is correlated with the north–south fluctuations of the three ocean fronts, with more detailed analysis in the case of the synoptic transient eddy heat flux and GS. The forcing and response causality is implied from the lag regressions as already explained in section 2d. The regression pattern with the atmosphere leading the ocean index is interpreted as the atmospheric pattern responsible for (i.e., forcing) the changes in the ocean front in subsequent years (i.e., the atmospheric forcing pattern). On the other hand, when the ocean index leads the atmosphere, the regression pattern is understood as the atmospheric pattern resulting from (i.e., responding to) the changes of the ocean fronts (i.e., the atmospheric response pattern).

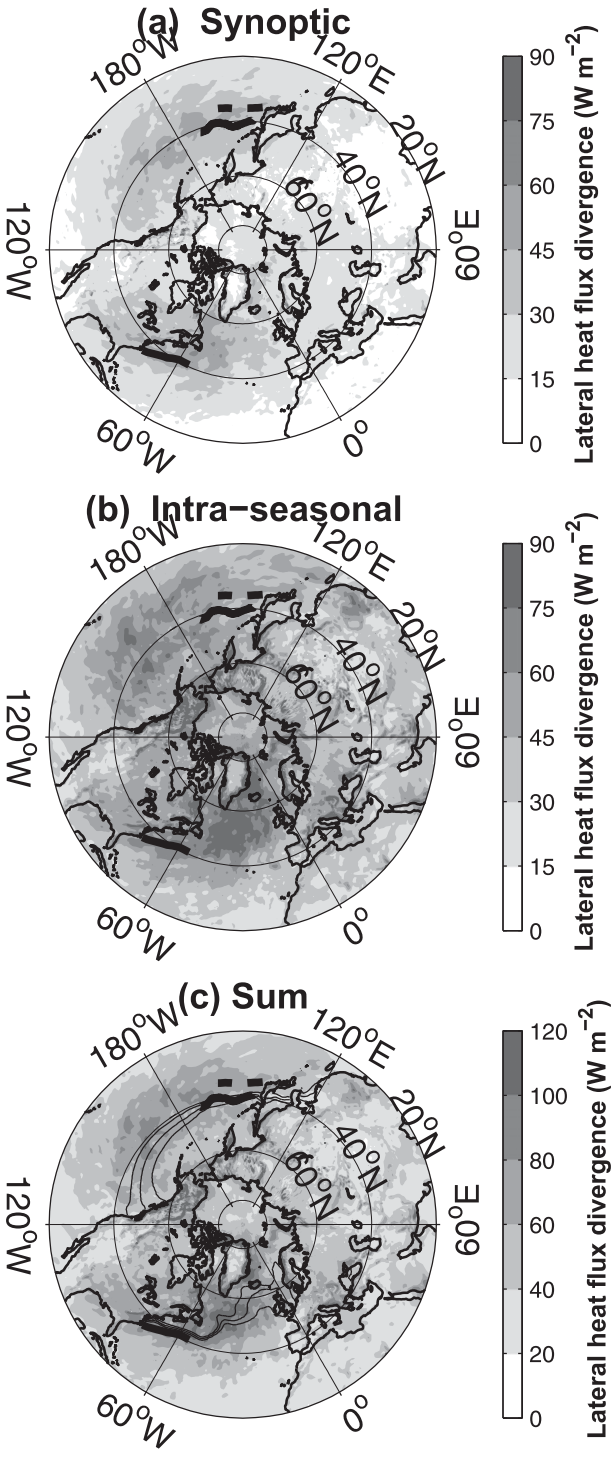

FIG. 7. Interannual standard deviation of 31 winter (JFM) mean vertically integrated lateral heat flux divergence by transient eddies as the sum of the sensible and latent components in the (a) synoptic band, (b) intraseasonal band, and (c) sum of two bands. Contour intervals are 15 W m^{-2} for the top two panels and 20 W m^{-2} for the bottom panel. Isotherms of the mean JFM SST for 6°, 8°, and 10°C are plotted with thin black lines. The mean positions of the GS and OE are indicated by thick black curves, and KE is indicated by thick dashed curves.

As already stated in the introduction, the primary emphasis of this subsection is how the changes in the ocean front position impact the atmospheric transient eddy fluxes, which can be shown based on the regression patterns when the atmosphere lags the ocean index. The regression patterns in the opposite lags (i.e., when the atmosphere leads) are also examined to aid the proper interpretation of the atmospheric response patterns. We have to keep in mind that the interpretation of the regression patterns when the atmosphere leads as the atmospheric forcing for the ocean front changes is only indirect. The atmospheric transient eddy heat fluxes do not directly drive the ocean circulation, but they are closely related to the storm track and large-scale atmospheric circulation, which in turn is associated with the basin-scale wind stress curl that drives the ocean circulation.

Figure 8 shows the lag regressions of the synoptic transient eddy fluxes (sensible + latent) on the GS index at six different lags from atmosphere leading by 3 yr to lagging by 2 yr. When the atmosphere leads the GS index by 1–3 yr, we see the anomalous atmospheric forcing associated with the storm track driving the meridional shift of the GS path (Figs. 8a–c). Note that the positive values for the GS index correspond to a northward shift of the GS relative to its mean position. Therefore, the significant positive regression anomalies to the north of the GS mean position in Figs. 8a–c indicate that the northward shift of the Atlantic storm track is associated with the atmospheric circulation change responsible for the northward shift of the GS in the following 1–3 yr, which is consistent with the wind-driven changes of the ocean circulation. The pattern is consistent for all three lags, and the amplitude is at maximum around 2–3 yr, which is slightly longer than previous estimates (Joyce et al. 2000; Frankignoul et al. 2001). This relationship is more clearly shown in Fig. 9a by adding (subtracting) the regression anomalies to (from) the mean synoptic transient eddy fluxes. We can see the storm track strengthens (weakens) as well as shifting northward (southward) prior to the northward (southward) shift of the GS.

When the GS index leads the transient eddy fluxes by either 1 or 2 yr (Figs. 8e–f), negative anomalies are found in farther downstream near the NAC. Again, the pattern is consistent between the two lags. Since the atmosphere lags the GS index by time scales much longer than the atmospheric intrinsic persistence time scale, the regression pattern is interpreted as the response to the changes in the ocean associated with the GS shift. This atmospheric response suggests that when the GS shifts to the north (south), the storm track becomes weaker (stronger) and contracts (extends) near the exit region of the Atlantic storm track (Fig. 9b). The amplitude of the anomalies in the atmospheric response

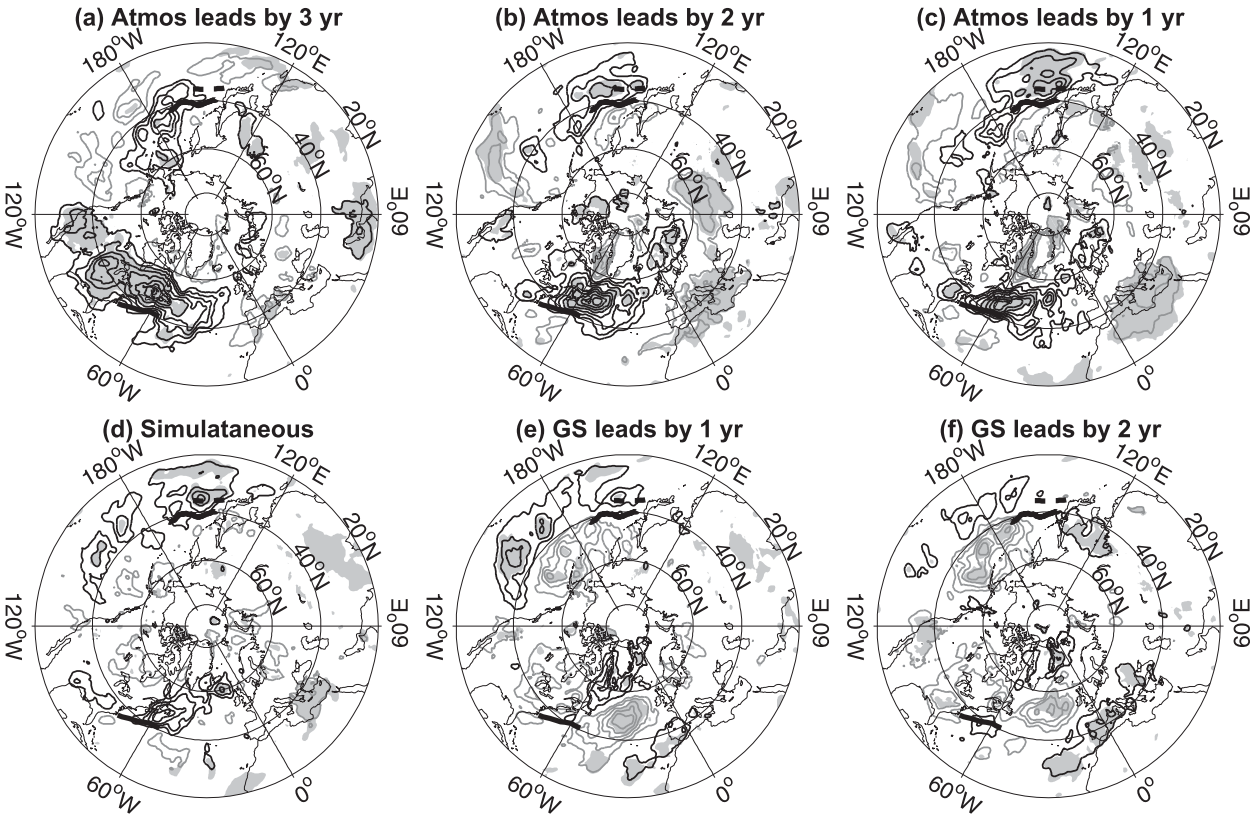

FIG. 8. Lag regressions of winter (JFM) vertically integrated meridional heat flux by synoptic transient eddies on the winter GSI. Positive (negative) regression coefficients are contoured with black (gray) lines. Zero contours are suppressed. Contour intervals are $0.2 \times 10^7\,\mathrm{W\,m^{-1}}$, and shadings indicate regression values significant at 90%. The mean positions of the GS and OE are indicated by thick black curves, and KE is indicated by thick dashed curve.

pattern is about ~40% of the interannual standard deviation in the synoptic transient eddy flux. On the other hand, that in the regression pattern associated with the atmospheric forcing is slightly greater.

For the GS shift to cause changes in the atmospheric circulation, it should communicate with the atmosphere through the SST and heat flux anomalies. Figure 10a exhibits that the large-scale positive SST anomalies form along the GS from the upstream near the Cape Hatteras to the east of the Grand Banks associated with the northward shift of the GS. The anomalies are coherent and wider in the downstream, even though the GS index is based on the region west of 55°W only. In addition to the positive anomalies along the ocean front, negative SST anomalies are also found along the western boundary and western half of the subpolar gyre, which is driven by the enhanced cyclonic gyre circulation and heat loss to the atmosphere in the subpolar North Atlantic associated with the positive phase of the NAO (Visbeck et al. 2003), which is also related to the northward shift of the storm track and GS at the same time. Therefore, the large-scale meridional dipole SST anomaly could effectively impact the atmospheric baroclinicity, hence the storm track. The maximum negative anomalies in the response pattern of the synoptic transient eddy heat flux (zoomed in from Fig. 8f to Fig. 10b) are located closely downstream of the positive SST anomalies. Note that the SST anomalies at lag = 0 are similar to those of lag = 1 yr, but the latter exhibits a slightly more expanded warm anomaly pattern along the GS, probably due to the mean advection of the anomalous SST.

The time series and autocorrelation for the JFM transient eddy flux near the maximum response region (40°–55°N, 10°–50°W) exhibit very different characteristics to those for the GS index (Figs. 11a–c). The transient eddy fluxes are dominated by year-to-year fluctuations and its autocorrelation drops to nearly zero within a year, which is typical for the midlatitude atmosphere. On the other hand, the GS index is dominated by decadal variability. The lag correlation between the two time series shows two peaks—that is, the positive peak when the atmosphere leads by 2 yr, representing the atmospheric forcing, and the negative peak when the GS leads by 1 yr, revealing the atmospheric response (Fig. 11d). The autocorrelation

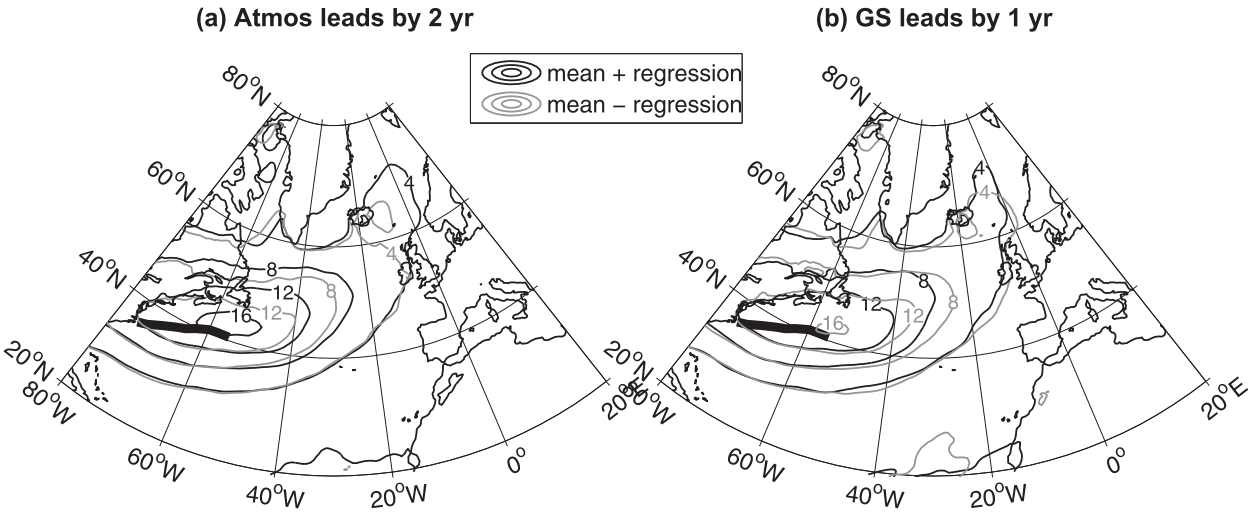

FIG. 9. Total winter (JFM) meridional heat fluxes by synoptic transient eddies corresponding to the ± one standard deviation changes in the winter GSI. Black (gray) contours are for the GS at the anomalously northern (southern) position—that is, the climatological winter mean shown in Fig. 1a plus (minus) the regression shown in (a) Fig. 8b and (b) Fig. 8e, respectively. Contour intervals are $4 \times 10^7\,\mathrm{W\,m^{-1}}$.

of the transient eddy heat flux has a curious negative peak at the 3-yr lag (Fig. 11b), which is not due to the tropical influence since the tropical influences are removed already. Considering the internal variability of the atmosphere to be white noise, it actually may be due to the response generated by the GS, which is 3 yr apart from the maximum forcing (Fig. 11d). However, the peak in the lag correlation in Fig. 11d when the GS leads by 1 yr barely misses being significant at the 90% level, though it is consistent with the other lag regression results (Figs. 8–10).

In addition, the vertical zonal sections of the atmospheric response and forcing averaged over 40°–55°N reveal very distinct structures. The forcing pattern (i.e., the regression when the atmosphere leads by 2 yr) exhibits the maximum near 850 hPa associated with the low-level storm track in 40°–70°W (Figs. 12a,c). In contrast, the response is farther downstream (20°–40°W) and penetrates into the upper troposphere (~300 hPa) with the maximum in 500–800 hPa (Fig. 12b). These distinctions suggest that the response pattern is not a statistical artifact due to periodicity in either variable.

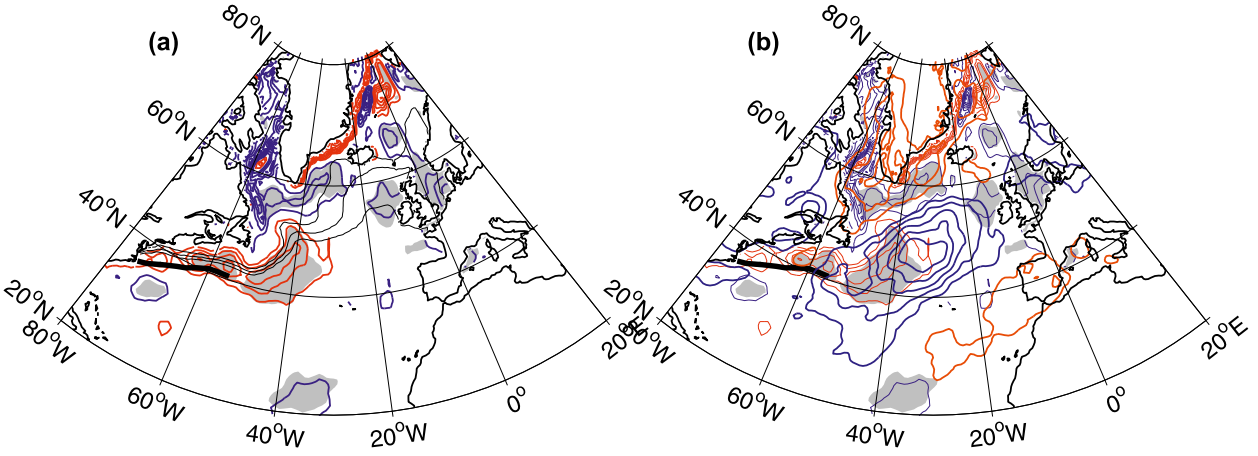

FIG. 10. Lag regressions of winter (JFM) SST on the winter GSI when the SST lags by 1 yr. Positive (negative) regression coefficients are contoured with red (blue) lines. Zero contours are suppressed. Contour intervals are 0.2°C, and shadings indicate regression values significant at 90%. (a) Isotherms of the mean JFM SST for 6°, 8°, and 10°C are plotted with the thin black line on top of the SST anomalies. (b) Orange (positive) and navy blue (negative) contours corresponding synoptic transient eddy meridional heat flux regression from Fig. 8e are added on top of the same SST anomalies.

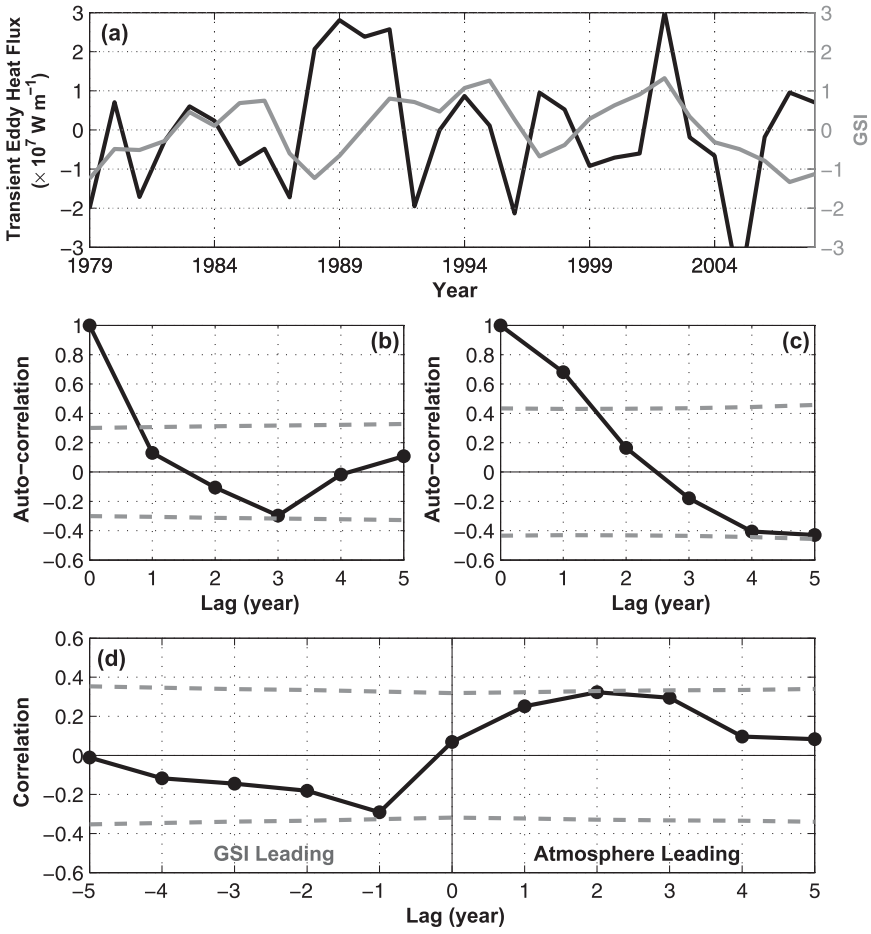

FIG. 11. (a) Winter (JFM) vertically integrated meridional heat flux by synoptic transient eddies averaged over 40°–55°N, 10°–50°W (black) and the winter GSI (gray) time series. (b) Autocorrelation of the synoptic transient eddy heat flux time series in (a). (c) Autocorrelation of the GSI. (d) Lag correlation between the synoptic transient eddy heat flux and GSI. The lag is positive when the transient eddy heat flux leads. Dashed lines indicate the 90% confidence interval.

Interestingly, the interannual root-mean-square values are slightly enhanced in the midtroposphere around 20°–40°W (Fig. 12d), collocated with the maximum response.

Note that there is an indication of an interbasin connection between the North Atlantic and North Pacific, both in the atmospheric lead/lag patterns, with a somewhat greater extent in the case of atmospheric lagging (Fig. 8). This is consistent with the fact that the GS and KE/OE indices are weakly correlated ($r = \sim 0.3$), as discussed already in section 2c. Of course, we have to keep in mind that the statistical significance is tested only at the 90% significance level.

The zonal integration of the regression anomalies for the transient eddy heat flux or equivalently the regression of the zonally integrated northward heat transport gives the anomalous northward heat transport by transient eddies associated with forcing for and response to the northward shift of the GS (Fig. 13a). When the atmosphere leads the northward GS shift, the northward heat transport increases to the north of the maximum heat transport latitude (~40°N) and slightly decreases to the south, thus reflecting the northward shift and increase of the maximum heat transport, consistent with the northward shift and intensification of the storm track in Figs. 8a–c and 9a. The equator-to-pole average of the anomalies is nonzero, which indicates the northward heat transport is amplified overall. (Note that lag = 1 yr is used here for consistency with the KE and OE cases discussed later, but lag = 2 yr gives a very similar result.) On the other hand, when the GS leads, the opposite is true. The heat transport decreases (slightly increases) to the north (south) of the maximum mean transport latitude for a northward (southward) GS excursion, which is consistent with reduced northward heat flux by the

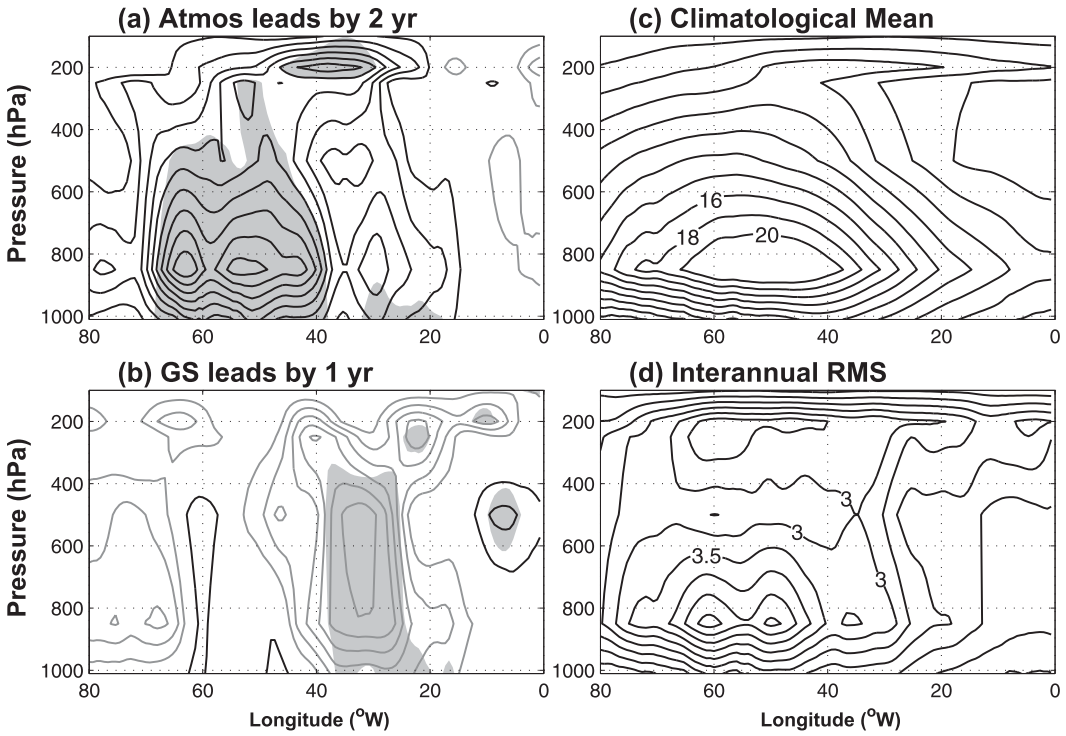

FIG. 12. (a),(b) Lag regressions of winter (JFM) meridional heat flux by synoptic transient eddies averaged for 40°–55°N on the winter GSI. Positive (negative) regression coefficients are contoured with black (gray) lines. Zero contours are suppressed. Contour intervals are 0.2×10^3 W m^{-2}, and shadings indicate regression values significant at 90%. (c) Climatological mean and (d) interannual standard deviation for the winter on the corresponding zonal section; Contour intervals are 2×10^3 and 0.5×10^3 W m^{-2}, respectively.

synoptic transient eddies near the exit region of the Atlantic storm track following the GS shifts northward (Figs. 8e,f and 9b).

Regression analyses are also done for the KE and OE indices with the synoptic transient eddy fluxes, which are only briefly reported here. Similar negative feedback patterns are found associated with the northward shift of the KE (i.e., positive eddy flux anomalies when the atmosphere leads and negative anomalies when the KE leads; Figs. 14a,b). The atmospheric forcing pattern (when the synoptic transient eddy fluxes lead by 1 yr; Fig. 14a) exhibits the northward shift of the storm tracks across the North Pacific and strengthening near the maximum prior to the northward shift of the KE. The interbasin connection to the North Atlantic is particularly strong in this case. Response patterns (when the KE leads by 1 yr; Fig. 14b) are opposite signed, and the significant anomalies are mostly confined near the KOE, while the maximum forcing anomalies are located downstream around the date line, which is consistent with the previous coupled model studies (Kwon and Deser 2007; Kwon et al. 2011). The associated zonally integrated northward heat transport (Fig. 13b) exhibits larger amplitude changes compared to the GS case, partly because of the pronounced interbasin connection and also the relatively larger width of the Pacific Ocean. Prior to the northward shift of the KE, the overall northward heat transport increases and shifts northward, while the overall amplitude decreases when the northward excursions of the KE lead.

For the regression on the OE index, the atmospheric forcing pattern (when the atmosphere leads by 1 yr; Fig. 14c) also suggests the northward shift of the storm track with intensification near the maximum, similar to the KE and GS cases. The response pattern clearly suggests the southward shift at least in the western North Pacific (Fig. 14d). The zonally integrated anomalous northward heat transports are also similar to the KE case (Fig. 13c).

In the intraseasonal time scale, both the atmospheric forcing and response patterns are very different from those in the synoptic time scale and are dominated by the smaller spatial scale with a hint of quasi-stationary waves (Fig. 15). The interaction between the intraseasonal transient eddies and the changes in the path of the ocean fronts seems distinct from that associated with the synoptic eddies, but the detail investigation is left for a follow-up study and we will only make a brief description here. The smaller spatial scale and the 90%

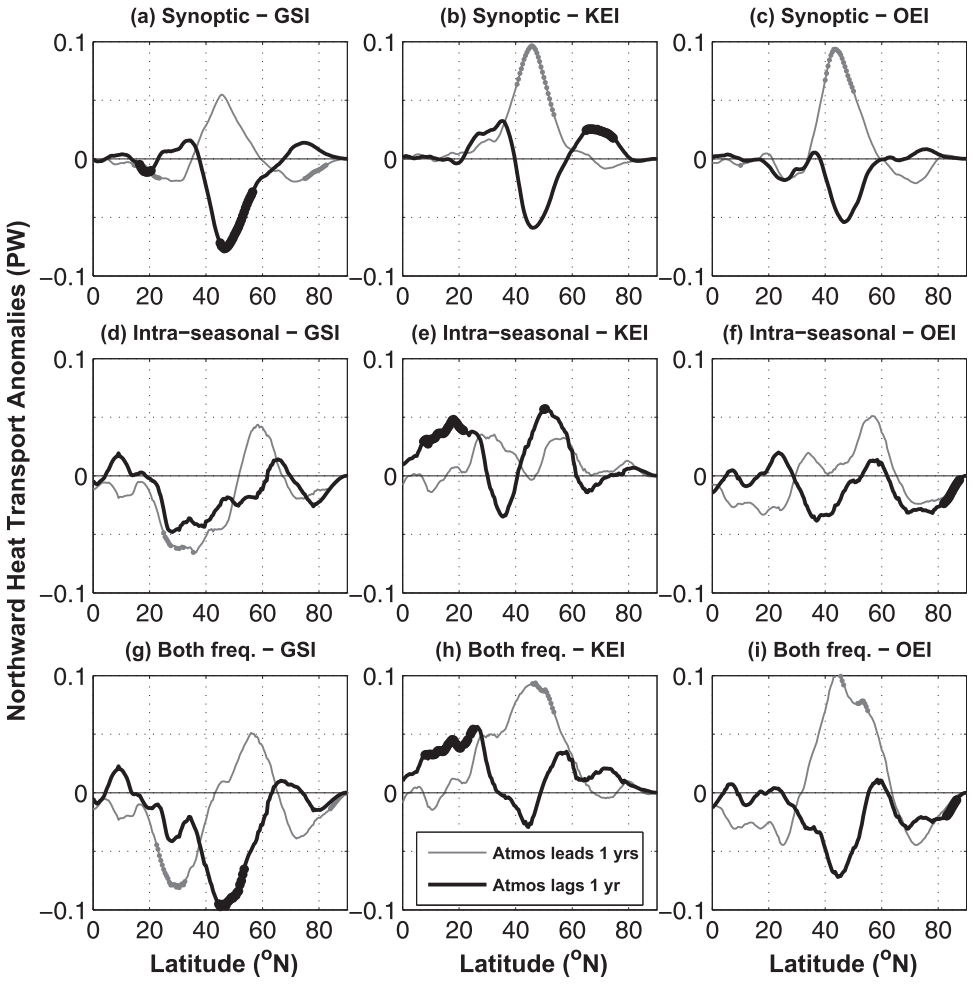

FIG. 13. Lag regressions of winter (JFM) zonally integrated northward heat transport by (top) synoptic, (middle) intraseasonal, and (bottom) synoptic + intraseasonal eddies on the (left) GSI, (center) KEI, and (right) OEI. The gray (black) lines are when the atmosphere leads (lags) the WBC indices by 1 yr. The thick parts of the regression curves indicate values significant at 90%. Note that the zonal integration of the heat fluxes are calculated circumglobally.

statistical significance level require caution in the interpretation of these patterns, especially the nonlocal anomalies. However, the anomalies driven by the western boundary current region heating may propagate remotely downstream in a quasi-stationary wavelike pattern (Kwon et al. 2011). The amplitude of the anomalies in the intraseasonal time scale is comparable or larger than that of the synoptic band and often dominates the sum of the two especially in the high latitudes near the Arctic (not shown). In some cases, the synoptic and intraseasonal transient eddy heat flux regression anomalies have the same sign locally (e.g., the positive anomalies near the GS and the negative anomalies near the Labrador Sea when the atmosphere leads the northward shift of the GS). The similar synergetic effect of the increased northward heat flux by transient eddies is seen in the North Pacific preceding the northward shift of the KE.

Zonal cancellation in the quasi-stationary wavelike anomalies results in slightly smaller zonally integrated anomalous northward heat transports by the intraseasonal transient eddies compared to those by the synoptic eddies, except for the case of the GS (Figs. 13d–f). However, the contribution from the intraseasonal band becomes dominant in the tropics and subtropics. The sums of the anomalous northward heat transports in the two frequency bands reach about ±0.1 PW in all three cases (Figs. 13g–i). Anomalies associated with the shift of GS show overall decrease in the northward heat transport both before and after the northward shift of the GS, while the anomalies associated with the KE and OE exhibit the changes in sign, though the regressions are hardly significant at 90%. These anomalous heat transports could add up or cancel out with each other depending on the relative phasing of the changes in three

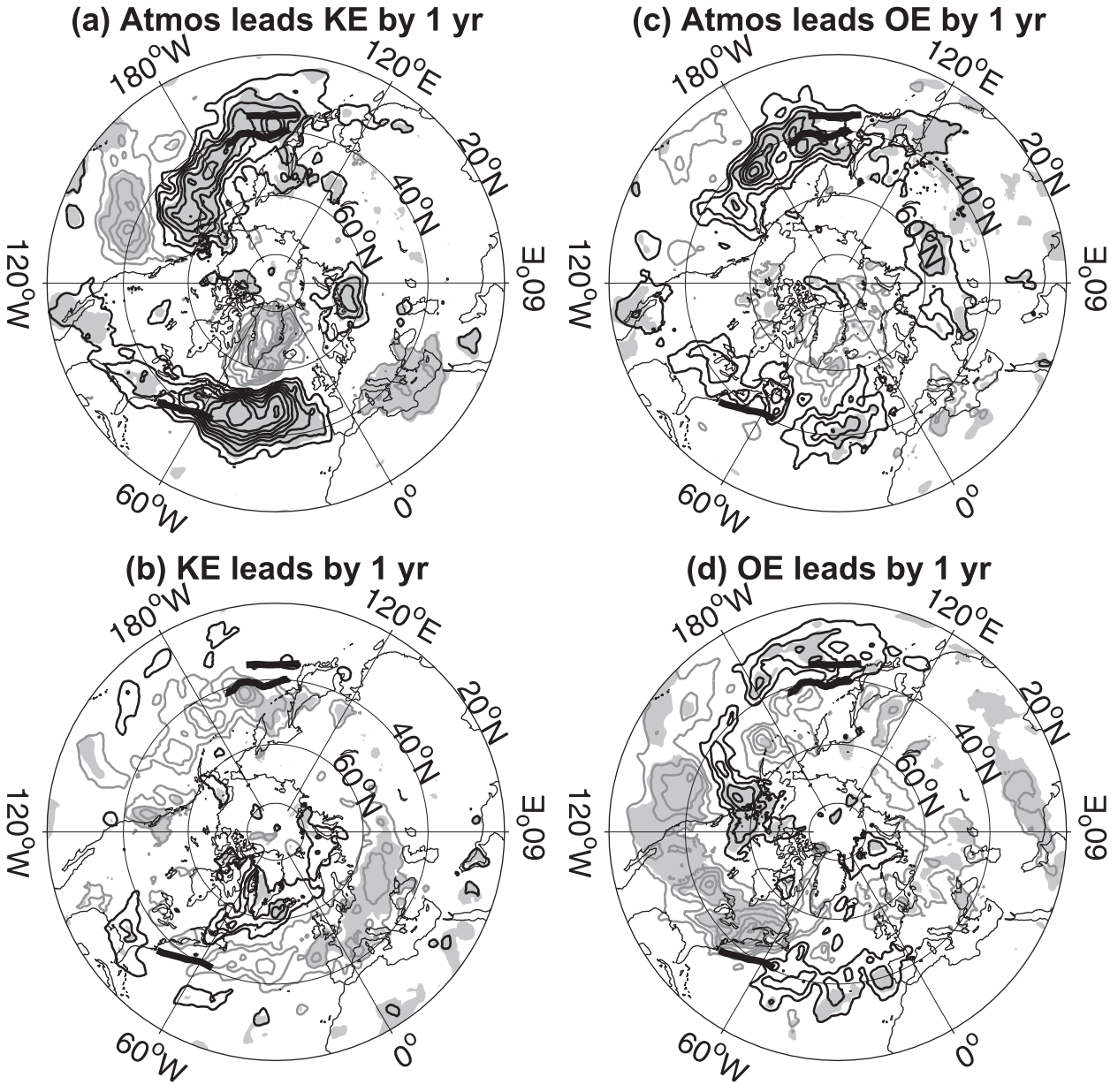

FIG. 14. Lag regressions of winter (JFM) vertically integrated meridional heat flux by synoptic transient eddies on the winter (a),(b) KEI and (c),(d) OEI. Positive (negative) regression coefficients are contoured with black (gray) lines. Zero contours are suppressed. Contour intervals are $0.2 \times 10^7\,\mathrm{W\,m^{-1}}$, and shadings indicate regression values significant at 90%. The mean positions of the GS and OE are indicated by thick black curves, and KE is indicated by thick dashed curve.

ocean fronts. In addition, the sum of these anomalies should be compensated by the sum of the seasonal-mean atmospheric heat transport (including contribution from the stationary eddies), net radiative flux at the top of the atmosphere, and the ocean heat transport.

4. Summary and discussion

We have examined the spatial and temporal covariability between the meridional heat fluxes by the atmospheric transient eddies in the Northern Hemisphere winter (January–March) and the paths of the three major ocean fronts in the western boundary current regions (i.e., GS, KE, and OE) for 1979–2009.

For the climatological mean, the northward heat fluxes by the synoptic transient eddies exhibited canonical storm tracks with their maximum amplitude collocated with the mean position of the GS and KE/OE in the North Atlantic and North Pacific, respectively. On the other hand, the intraseasonal counterpart showed a very

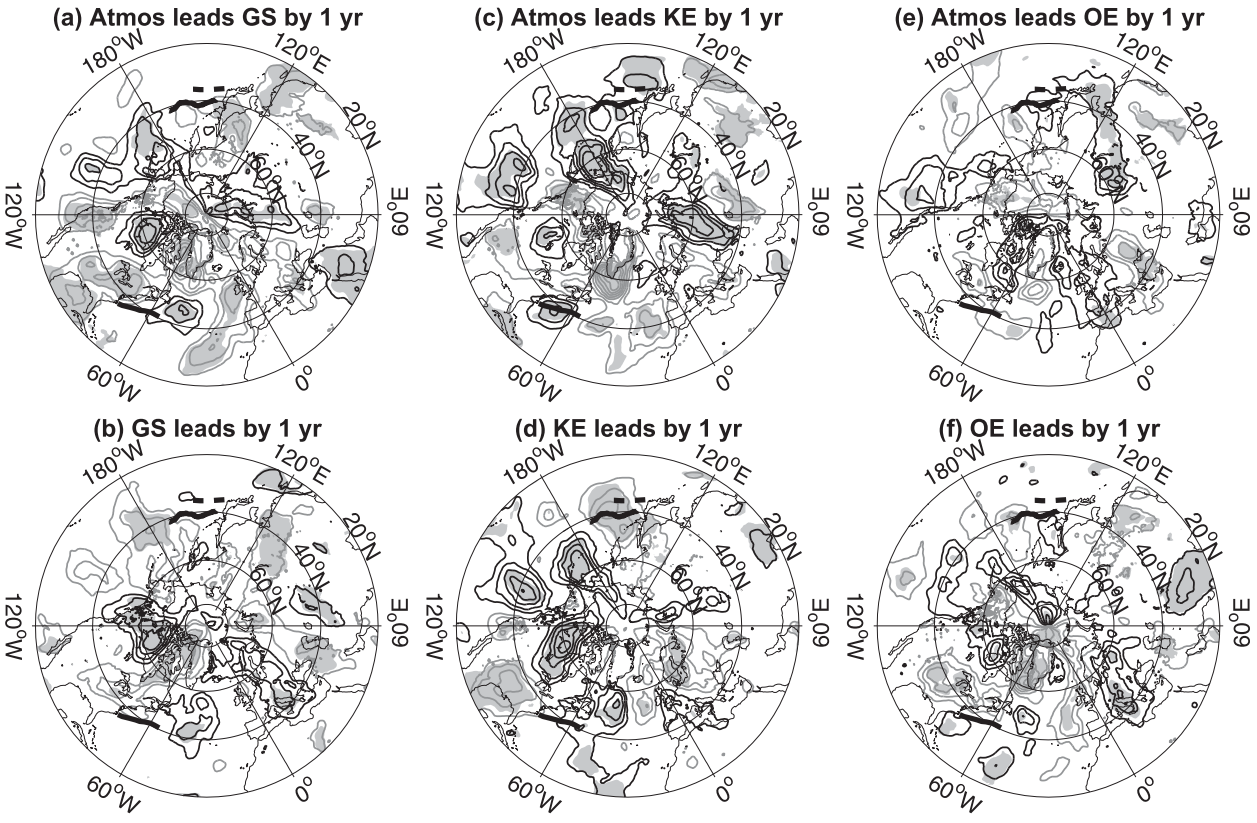

FIG. 15. Lag regressions of winter (JFM) vertically integrated meridional heat flux by intraseasonal transient eddies on the winter (a),(b) GSI, (c),(d) KEI, and (e),(f) OEI. Positive (negative) regression coefficients are contoured with black (gray) lines. Zero contours are suppressed. Contour intervals are 0.5×10^7 W m^{-1}, and shadings indicate regression values significant at 90%. The mean positions of the GS and OE are indicated by thick black curves, and KE is indicated by thick dashed curve.

different spatial pattern with more localized maximum near the major orographic features and near the blocking regions, primarily associated with the AO and PNA variability. The mean spatial pattern of the lateral divergence of vertically integrated heat fluxes by transient eddies revealed distinct contributions from the synoptic and intraseasonal bands, while the sum of the two frequency bands exhibits very close coupling with the exact locations of the ocean fronts.

Linear regression was used to examine the lead–lag relationship between the interannual changes in the northward heat fluxes by the transient eddies and the changes in the paths of the GS, KE, and OE, respectively. One to three years prior to the northward shifts of each ocean front, the atmospheric storm track shifted northward and intensified, which is consistent with the wind-driven changes of the ocean circulation as the northward shift of the storm track is associated with the northward shift of the wind stress curl. While the changes in the atmospheric transient eddy heat fluxes were concentrated near the storm-track maxima when the atmosphere led, the anomalies were primarily found near the downstream storm-track exit region following the ocean changes. After northward shifts of the ocean fronts, the synoptic storm tracks weakened in all three cases. In terms of the zonally integrated northward heat transport by the atmospheric synoptic transient eddies, the heat transport increased by ~5% of its maximum mean value prior to the northward shift of each ocean front and decreased to a similar amplitude following the ocean front shifts.

a. Ocean-to-atmosphere feedback in the lateral heat flux divergence

Perhaps the clearest evidence of ocean-to-atmosphere feedback presented in this paper is in the climatological mean spatial pattern of the lateral heat flux divergence by transient eddies (Fig. 5). As Seager et al. (2002) articulated, the atmospheric circulation (synoptic plus quasi-stationary intraseasonal eddies in our study) defines the basin-scale heat flux divergence pattern (i.e., the atmosphere is heated by the warm subtropical ocean and carries heat to the colder subpolar and Arctic regions). However, the detailed spatial pattern of the boundary between the atmospheric heat flux divergence and

convergence regions (for the sum of the synoptic and intraseasonal bands) tracking the ocean fronts is too fine a scale to be set by the atmospheric circulation alone.

More specifically, the northern edge of the heat flux divergence region (reddish shading in Fig. 5c) in the North Atlantic tracks remarkably well the NAC front marked by three SST isotherms. The match between the two, along the paths of ocean currents (e.g., the Northwest Corner, the separation near the Flemish Cap, and then the North Atlantic Drift over the Mid-Atlantic Ridge), is primarily guided by the ocean bathymetry. Even in the North Pacific where the topographic steering of the KE and OE currents is not as dramatic as the North Atlantic, there may be a hint of KE meandering imprinted on the lateral heat flux divergence with the wavy zero divergence region between the coast of Japan and the date line. This result strongly suggests the ocean front determines the position of the atmospheric storm track not only for the synoptic eddies near the strong SST front in the western basin (cf. Nakamura et al. 2004) but also for the low-frequency eddies around the relatively weaker SST front in the eastern basin, of which implication is further discussed in the next subsection.

It is worth being reminded that the lateral heat flux divergence is calculated for the whole atmospheric column vertically integrated from the surface to 50 hPa. Therefore, if the atmospheric internal variability in the upper-level jet dominantly shapes the pattern, there should not be such a close correspondence between the lateral heat flux divergence pattern and the ocean fronts. Instead, the lateral heat flux by the transient eddies and its divergence are dominated by the contribution from the lower-level jet (Fig. 3), which could be more strongly coupled to the underlying ocean. A similar seamless pattern is hinted in Fig. 4 of Trenberth and Stepaniak (2003b), though they did not emphasize the role of the ocean fronts.

b. Intraseasonal transient eddies

While strong evidence of the atmospheric transient eddies feeling the underlying SST front is presented, the mechanism is not clear. Previous studies suggested mechanisms for ocean-to-atmosphere feedback to the synoptic transient eddies near a strong ocean front (Hoskins and Valdes 1990; Nakamura et al. 2004). However, our results suggest not only the synoptic eddies but also the intraseasonal eddies are impacted by the existence of the ocean fronts, especially in the eastern North Atlantic (Figs. 5b,c).

This region coincides with one of the major blocking regions in the Northern Hemisphere (Tyrlis and Hoskins 2008). Recently, Häkkinen et al. (2011) reported that the occurrence frequency of the North Atlantic blocking, one of the most prominent intraseasonal weather phenomena in the extratropics, shows a prominent multidecadal variability in phase with the Atlantic multidecadal variability (AMV; also often called Atlantic multidecadal oscillation). They focused on the role of blocking anticyclones in driving changes in ocean circulation associated with the AMV. Perhaps an even more intriguing open question would be why the blocking, an intraseasonal weather phenomena, exhibits such a multidecadal variability, to what extent the ocean-to-atmosphere feedback plays a role, and whether the AMV is a resulting coupled ocean–atmosphere mode of variability (Woolings 2011).

Our result provides a piece of evidence for a significant ocean-to-atmosphere feedback associated with the intraseasonal transient eddies at least in the mean sense. Furthermore, the GS position index used in this study extends back to 1954 and contains a significant multidecadal variability, although only the 1979–2006 portion is used in this study (Joyce et al. 2000). However, the lead–lag regressions for the interannual variability of the intraseasonal transient eddy heat flux and the ocean fronts were difficult to interpret (Fig. 15a). Relatively heterogeneous spatial patterns, larger variability, and inherently longer time scales in the intraseasonal band (compared to the synoptic band) result in a smaller signal-to-noise ratio. Therefore, a further careful investigation is needed for the ocean-to-atmosphere feedback in the intraseasonal time scale. In particular, the dynamical link between the synoptic and intraseasonal eddies and their response to the ocean front needs to be clarified [e.g., by examining how the convergence of the synoptic eddy vorticity flux is collocated with the intraseasonal eddies; Nakamura et al. (1997)]. Perhaps an atmospheric general circulation model with specified SST anomalies associated with the ocean front changes may be useful. In addition to coupling through heat fluxes, the ocean–atmosphere feedback through momentum exchanges may also play important role, especially driving ocean circulation changes.

c. Ocean–atmosphere coupling and decadal climate variability

In addition to the intriguing possibility of the ocean–atmosphere coupling through the intraseasonal blocking to drive the AMV, our results suggest that the ocean–atmosphere coupling could be active for the interannual-to-decadal variability in both the North Atlantic and North Pacific.

The lead–lag relationship between the synoptic transient eddy northward heat flux and the GS path suggests

that the atmospheric patterns preceding the northward shift of the GS and those following are overall opposite signed, and their maximum anomalies are separated by ~3 yr, which implies a weak ~6-yr oscillatory mode due to ocean–atmosphere coupling. Perhaps, the relatively high-frequency-dominated (around 5 yr) NAO variability in the recent 3 decades could be associated with our observations.

Similar opposite-signed regression patterns were found associated with the KE and OE variability. Previous studies primarily based on climate models also suggested an ocean–atmosphere coupled mode responsible for the decadal variability in the North Pacific, which involves opposite-signed atmospheric circulation preceding and following the KE changes (Pierce et al. 2001; Kwon and Deser 2007). On the other hand, Frankignoul et al. (2011) showed that atmospheric forcing and response patterns associated with the meridional shift of the OE have the same sign and may be related to a North Pacific Oscillation (NPO)-like pattern, which implies a positive feedback, instead.

Previous studies on the midlatitude ocean–atmosphere coupled mode are almost exclusively based on the low-frequency variability of monthly or seasonal mean values. On the other hand, our results are based on the low-frequency variability of the synoptic and intraseasonal variances. In addition, our result hints at a possible link to the Bjerknes compensation, which suggests anomalies of oceanic and atmospheric meridional energy transport should be equal and opposite (Bjerknes 1964). However, this speculation can only be confirmed by further examining the atmospheric terms not included in this study, for example, stationary eddy heat fluxes and the ocean heat transport at the same time.

d. Seasonality

We have focused only on the three winter months (January–March) in this study. JFM exhibits the strongest northward heat fluxes and northward heat transports through the transient eddies (not shown). The October–December transient eddy heat fluxes and heat transports are nearly as strong as the JFM ones, while the minimum heat fluxes and transports are in July–September with their maximum amplitude reaching only 50%–60% of JFM's maximum. Since the atmospheric and ocean circulation exhibit a strong seasonal cycle, covariability between the two could also have seasonality. In-depth analysis of the seasonal dependency in this paper is left for a future study.

Acknowledgments. Support from the National Aeronautics and Space Administration (NASA) Physical Oceanography Program (NNX09AF35G to TJ and Y-OK) and the Department of Energy (DOE) Climate and Environmental Sciences Division (DE-SC0007052 to Y-OK) is gratefully acknowledged. The authors also acknowledge the NASA Global Modeling and Assimilation Office (GMAO) and the Goddard Earth Sciences Data and Information Services Center (GES DISC) for the dissemination of MERRA and John Fasullo for initially providing the daily mean data. We are very grateful for the helpful discussions with many colleagues including Mike Alexander, Richard Cullather, Clara Deser, John Fasullo, Claude Frankignoul, Guillaume Gastineau, Hisashi Nakamura, Matt Newman, and Justin Small and the thorough reviews by the three anonymous reviewers.

REFERENCES

Bjerknes, J., 1964: Atlantic air-sea interaction. *Advances in Geophysics,* Vol. 10, Academic Press, 1–82.

Blackmon, M. L., 1976: A climatological spectral study of the 500 mb geopotential height of the Northern Hemisphere. *J. Atmos. Sci.,* **33,** 1607–1623.

——, J. M. Wallace, N.-C. Lau, and S. L. Mullen, 1977: An observational study of the Northern Hemisphere wintertime circulation. *J. Atmos. Sci.,* **34,** 1040–1053.

——, Y.-H. Lee, J. M. Wallace, and H.-H. Hsu, 1984: Time variation of 500 mb height fluctuations with long, intermediate and short time scales as deduced from lag-correlation statistic. *J. Atmos. Sci.,* **41,** 981–991.

Boyer, T. P., and Coauthors, 2009: *World Ocean Database 2009.* S. Levitus, Ed., NOAA Atlas NESDIS 66, 216 pp.

Bretherton, C. S., M. Widman, V. P. Dymnikov, J. M. Wallace, and I. Bladé, 1999: The effective number of spatial degrees of freedom of a time-varying field. *J. Climate,* **12,** 1990–2009.

Chang, E. K. M., S. Lee, and K. L. Swanson, 2002: Storm track dynamics. *J. Climate,* **15,** 2163–2183.

Deser, C., M. A. Alexander, and M. S. Timlin, 1999: Evidence for a wind-driven intensification of the Kuroshio Current extension from the 1970s to the 1980s. *J. Climate,* **12,** 1697–1706.

Dole, R. M., and R. X. Black, 1990: Life cycles of persistent anomalies. Part II: The development of persistent negative height anomalies over the North Pacific Ocean. *Mon. Wea. Rev.,* **118,** 824–846.

Duchon, C. E., 1979: Lanczos filtering in one and two dimensions. *J. Appl. Meteor.,* **18,** 1016–1022.

Frankignoul, C., and E. Kestenare, 2002: The surface heat flux feedback. Part I: Estimates from observations in the Atlantic and the North Pacific. *Climate Dyn.,* **19,** 633–647.

——, A. Czaja, and B. L'Heveder, 1998: Air–sea feedback in the North Atlantic and surface boundary conditions for ocean models. *J. Climate,* **11,** 2310–2324.

——, G. de Coëtlogon, T. M. Joyce, and S. Dong, 2001: Gulf Stream variability and ocean–atmosphere interactions. *J. Phys. Oceanogr.,* **31,** 3516–3529.

——, N. Sennéchael, Y.-O. Kwon, and M. A. Alexander, 2011: Atmosphere–ocean variability associated with Kuroshio and Oyashio Extension fluctuations. *J. Climate,* **24,** 762–777.

Häkkinen, S., P. B. Rhines, and D. L. Worthen, 2011: Atmospheric blocking and Atlantic multidecadal ocean variability. *Science,* **334,** 655–659.

Hoskins, B. J., and P. J. Valdes, 1990: On the existence of storm-tracks. *J. Atmos. Sci.,* **47,** 1854–1864.

——, and K. I. Hodges, 2002: New perspectives on the Northern Hemisphere winter storm tracks. *J. Atmos. Sci.,* **59,** 1041–1061.

Jayne, S. R., and J. Marotzke, 2002: The oceanic eddy heat transport. *J. Phys. Oceanogr.,* **32,** 3328–3345.

Johns, W. E., and Coauthors, 2011: Continuous, array-based estimates of Atlantic Ocean heat transport at 26.5°N. *J. Climate,* **24,** 2429–2449.

Joyce, T. M., and R. Zhang, 2010: On the path of the Gulf Stream and the Atlantic meridional overturning circulation. *J. Climate,* **23,** 3146–3154.

——, C. Deser, and M. A. Spall, 2000: The relation between decadal variability of subtropical mode water and the North Atlantic Oscillation. *J. Climate,* **13,** 2550–2569.

——, Y.-O. Kwon, and L. Yu, 2009: On the relationship between synoptic wintertime atmospheric variability and path shifts in the Gulf Stream and Kuroshio Extension. *J. Climate,* **22,** 3177–3192.

Kelly, K. A., R. J. Small, R. M. Samelson, B. Qiu, T. M. Joyce, Y.-O. Kwon, and M. Cronin, 2010: Western boundary currents and frontal air–sea interaction: Gulf Stream and Kuroshio Extension. *J. Climate,* **23,** 5644–5667.

Kushnir, Y., and J. M. Wallace, 1989: Low-frequency variability in the Northern Hemisphere winter: Geographical distribution, structure and time-scale dependence. *J. Atmos. Sci.,* **46,** 3122–3143.

Kwon, Y.-O., and C. Deser, 2007: North Pacific decadal variability in the Community Climate System Model version 2. *J. Climate,* **20,** 2416–2433.

——, M. A. Alexander, N. A. Bond, C. Frankignoul, H. Nakamura, B. Qiu, and L. Thompson, 2010: Role of Gulf Stream and Kuroshio–Oyashio systems in large-scale atmosphere–ocean interaction: A review. *J. Climate,* **23,** 3249–3281.

——, C. Deser, and C. Cassou, 2011: Coupled atmosphere–mixed layer ocean response to ocean heat flux convergence along the Kuroshio Current extension. *Climate Dyn.,* **36,** 2295–2312, doi:10.1007/s00382-010-0764-8.

Lorenz, E. N., 1967: The nature and theory of the general circulation of the atmosphere. WMO Rep. 218, 161 pp.

Minobe, S., A. Kuwano-Yoshida, N. Komori, S.-P. Xie, and R. J. Small, 2008: Influence of the Gulf Stream on the troposphere. *Nature,* **452,** 206–209.

——, M. Miyashita, A. Kuwano-Yoshida, H. Tokinaga, and S.-P. Xie, 2010: Atmospheric response to the Gulf Stream: Seasonal variations. *J. Climate,* **23,** 3699–3719.

Nakamura, H., and J. M. Wallace, 1990: Observed changes in baroclinic wave activity during the life cycles of low-frequency circulation anomalies. *J. Atmos. Sci.,* **47,** 1100–1116.

——, M. Nakamura, and J. L. Anderson, 1997: The role of high- and low-frequency dynamics and blocking formation. *Mon. Wea. Rev.,* **125,** 2074–2093.

——, T. Sampe, Y. Tanimoto, and A. Shimpo, 2004: Observed associations among storm tracks, jet streams and midlatitude oceanic fronts. *Earth's Climate: The Ocean–Atmosphere Interaction, Geophys. Monogr.,* Vol. 147, Amer. Geophys. Union, 329–346.

Newman, M., G. N. Kiladis, K. M. Weickmann, F. M. Ralph, and P. D. Sardeshmukh, 2012: Relative contributions of synoptic and low-frequency eddies to time-mean atmospheric moisture transport, including the role of atmospheric rivers. *J. Climate,* **25,** 7341–7361.

Nonaka, M., H. Nakamura, Y. Tanimoto, T. Kagimoto, and H. Sasaki, 2006: Decadal variability in the Kuroshio–Oyashio Extension simulated in an eddy-resolving OGCM. *J. Climate,* **19,** 1970–1989.

——, ——, ——, ——, and ——, 2008: Interannual-to-decadal variability in the Oyashio and its influence on temperature in the subarctic frontal zone: An eddy-resolving OGCM simulation. *J. Climate,* **21,** 6283–6303.

Peixoto, J. P., and A. H. Oort, 1992: *Physics of Climate.* American Institute of Physics Press, 520 pp.

Peña-Molino, B., and T. M. Joyce, 2008: Variability in the slope water and its relation to the Gulf Stream path. *Geophys. Res. Lett.,* **35,** L0306, doi:10.1029/2007GL032183.

Pierce, D. W., T. P. Barnett, N. Schneider, R. Saravanan, D. Dommenget, and M. Latif, 2001: The role of ocean dynamics in producing decadal climate variability in the North Pacific. *Climate Dyn.,* **18,** 51–70.

Priestley, C. H. B., 1949: Heat transport and zonal stress between latitudes. *Quart. J. Roy. Meteor. Soc.,* **75,** 28–40.

Qiu, B., 2002: The Kuroshio Extension system: Its large-scale variability and role in the midlatitude ocean-atmosphere interaction. *J. Oceanogr.,* **58,** 57–75.

——, and S. Chen, 2005: Variability of the Kuroshio Extension jet, recirculation gyre and mesoscale eddies on decadal timescales. *J. Phys. Oceanogr.,* **35,** 2090–2103.

——, N. Schneider, and S. Chen, 2007: Coupled decadal variability in the North Pacific: An observationally constrained idealized model. *J. Climate,* **20,** 3602–3620.

Raphael, M. N., 1997: The relationship between the transient, meridional eddy sensible and latent heat flux. *J. Geophys. Res.,* **102** (D12), 13 487–13 494.

Reynolds, R. W., T. M. Smith, C. Liu, D. B. Chelton, K. S. Casey, and M. G. Schlax, 2007: Daily high-resolution-blended analyses for sea surface temperature. *J. Climate,* **20,** 5473–5496.

Rienecker, M. M., and Coauthors, 2011: MERRA: NASA's Modern-Era Retrospective Analysis for Research and Applications. *J. Climate,* **24,** 3624–3648.

Sasaki, Y. N., S. Minobe, T. Asai, and M. Inatsu, 2012: Influence of the Kuroshio in the East China Sea on the early summer (baiu) rain. *J. Climate,* **25,** 6627–6645.

Seager, R., Y. Kushnir, N. H. Naik, M. A. Cane, and J. Miller, 2001: Wind-driven shifts in the latitude of the Kuroshio–Oyashio Extension and generation of SST anomalies on decadal timescales. *J. Climate,* **14,** 4249–4265.

——, D. S. Battisti, J. Yin, N. Gordon, N. H. Naik, A. C. Clement, and M. A. Cane, 2002: Is the Gulf Stream responsible for Europe's mild winters? *Quart. J. Roy. Meteor. Soc.,* **128,** 2563–2586.

Taguchi, B., H. Nakamura, M. Nonaka, and S.-P. Xie, 2009: Influences of the Kuroshio/Oyashio Extensions on air–sea heat exchanges and storm-track activity as revealed in regional atmospheric model simulations for the 2003/04 cold season. *J. Climate,* **22,** 6536–6560.

Toginaga, H., Y. Tanimoto, S.-P. Xie, T. Sampe, H. Tomita, and H. Ichikawa, 2009: Ocean frontal effects on the vertical development of clouds over the western North Pacific: In situ and satellite observations. *J. Climate,* **22,** 4241–4260.

Trenberth, K. E., 1984: Some effects of finite sample size and persistence on meteorological statistics. Part I: Autocorrelations. *Mon. Wea. Rev.,* **112,** 2359–2368.

——, and J. M. Caron, 2001: Estimates of meridional atmosphere and ocean heat transports. *J. Climate,* **14,** 3433–3443.

——, and D. P. Stepaniak, 2003a: Covariability of components of poleward atmospheric energy transports on seasonal and interannual timescales. *J. Climate,* **16,** 3691–3705.

——, and ——, 2003b: Seamless poleward atmospheric energy transports and implications for the Hadley circulation. *J. Climate,* **16,** 3706–3722.

Tyrlis, E., and B. J. Hoskins, 2008: Aspects of a Northern Hemisphere atmospheric blocking climatology. *J. Atmos. Sci.,* **65,** 1638–1652.

Visbeck, M., E. P. Chassignet, R. G. Curr, T. L. Delworth, R. R. Dickson, and G. Krahmann, 2003: The ocean's response to North Atlantic Oscillation variability. *The North Atlantic Oscillation: Climatic Significance and Environmental Impact, Geophys. Monogr.,* Vol. 134, Amer. Geophys. Union, 113–145.

Volkov, D. L., T. Lee, and L. L. Fu, 2008: Eddy-induced meridional heat transport in the ocean. *Geophys. Res. Lett.,* **35,** L20601, doi:10.1029/2008GL035490.

von Storch, J.-S., 2000: Signatures of air–sea interactions in a coupled atmosphere–ocean GCM. *J. Climate,* **13,** 3361–3379.

Woolings, T., 2011: Ocean effects of blocking. *Science,* **334,** 612–613.

Xu, H., M. Xu, S.-P. Xie, and Y. Wang, 2011: Deep atmospheric response to the spring Kuroshio over the East China Sea. *J. Climate,* **24,** 4959–4972.

Yasuda, I., 2003: Hydrographic structure and variability in the Kuroshio-Oyashio transition area. *J. Oceanogr.,* **59,** 389–402.